Journal of Materials Chemistry A

ROYAL SOCIETY OF CHEMISTRY

PAPER

View Article Online
View Journal

Check for updates

Cite this: DOI: 10.1039/d5ta08349d

Detonation nanodiamonds with ultrapure surfaces through a combined chlorine and fluorine gas treatment

Killian Henry,[ab] Mélanie Emo,[a] Sébastien Diliberto,[a] Sébastien Hupont,[a] Julien Parmentier,[c] Sylvette Brunet,[d] Jean-Dominique Comparot,[d] Marc Dubois[b] and Brigitte Vigolo *[a]

Achieving a highly purified surface of nanodiamonds of a calibrated size is of great interest considering the wide range of applications requiring perfect control for maximizing their properties and resulting performance. However, existing purification methods, involving strong acids and oxidants, suffer from a lack of selectivity because they can attack nanodiamonds and add new contaminants to the sample. In this work, a highly selective gas-phase approach that combines two halogen gases (chlorine and fluorine) is successfully developed. First, a treatment under elemental chlorine at 650 °C for 1 h is able to remove all inorganic impurities except silica. Second, a thermal treatment under elemental fluorine (at 520 °C for 12 h) is used to eliminate both silica and surface impurities (disorganized sp^2 layers and oxygen- and hydrogen-containing functional groups) from size-calibrated detonation nanodiamonds. The resulting cleaned diamond surface is covered by carbon–fluorine bonds only. An in-depth investigation using several complementary techniques, including *in situ* characterizations, allows determination of the chemical reactions playing a major role in the manifested highly efficient impurity removal. The formation of fluorinated gases such as HF, CF_4, and C_2F_6 is evidenced along with that of silicon fluorides such as SiF_4. The role of fluorine as a stabilizing ("passivating") agent for the surface is proposed by comparison with fluorinated diamane. These detonation nanodiamonds with an ultrapure surface show remarkable thermal stability, with a combustion temperature up to 225 °C higher than that of raw detonation nanodiamonds. These findings open the way to broadly extend the use of detonation nanodiamonds for applications requiring harsh reaction conditions, for which most nanomaterials are strongly limited.

Received 13th October 2025
Accepted 20th February 2026

DOI: 10.1039/d5ta08349d

rsc.li/materials-a

Open Access Article. Published on 24 February 2026. Downloaded on 3/17/2026 1:39:49 PM.
This article is licensed under a Creative Commons Attribution 3.0 Unported Licence.

1 Introduction

The synthesis of nanodiamonds produced by detonation, the so-called detonation nanodiamonds (DNDs), was reported for the first time in the 1960s. DNDs, which are unique owing to their structure, shape and properties, are of great interest since they possess a calibrated size of 4–5 nm, and they can be synthesized in large quantities. They have the potential to be used in a myriad of applications owing to their versatility regarding surface chemistry modification and their thermal and chemical stability: supercapacitors, heat transfer fluids, bioapplications like imaging, neutron science, and lubricants.[1–12] DNDs contain several kinds of impurities in varying amounts located (i) inside the sp^3 diamond core of DNDs or (ii) in the near-surface region of DNDs in between the DND particles embedded in agglomerates they naturally form. (i) During ultrafast detonation synthesis, a limited fraction of nitrogen originating from nitrogen-rich explosives (*e.g.* trinitrotoluene (TNT) and hexogen (RDX)) is incorporated substitutionally into the diamond sp^3 core of DNDs, forming isolated paramagnetic centers (PCs) of different types localized within the nanodiamond particles. Even at a low concentration of 0.4–2.0 at%, these internal DND impurities are of great interest because they induce peculiar optical properties and their impact on the other exploitable properties is negligible. This is the reason why, when a purification method is applied to DNDs, their removal is usually not desired, and their accessibility is also dramatically limited. (ii) Non-internal impurities are of several types, including inorganic impurities mainly based on SiO_2, Cr- or Fe-based nanoparticles, and poorly graphitized sp^2 layers functionalized with oxygenated and hydrogenated

[a]Université de Lorraine, CNRS, IJL, F-54000 Nancy, France. E-mail: Brigitte.Vigolo@univ-lorraine.fr

[b]Université Clermont Auvergne, CNRS, ICCF UMR 6296, 24 av. Blaise Pascal, F-63178 Aubière, France

[c]Université de Strasbourg, Université de Haute-Alsace, Institut de Science des Matériaux de Mulhouse (IS2M), UMR 7361 CNRS-UHA, 15 rue Jean Starcky, BP 2488, 68057 Mulhouse Cedex, France

[d]Institut de Chimie des Milieux et Matériaux de Poitiers - IC2MP 7285, UMR CNRS, 4 rue Michel Brunet, 86073 Poitiers Cedex 9, France

Open Access Article. Published on 24 February 2026. Downloaded on 3/17/2026 1:39:49 PM.
This article is licensed under a Creative Commons Attribution 3.0 Unported Licence.

surface groups.[3,11,13–17] Regardless of their nature, each of these external impurities located on the external surface of DNDs can negatively impact the targeted property that needs to be exploited for further designing DND-based added-value materials or devices. It is widely recognized that the resulting intrinsic variability of DNDs severely limits the possibility of precisely controlling and tuning DND properties. As a consequence, at the current stage, a reliable transfer of the DNDs to practical applications for developing new technologies remains far below the possibilities demonstrated at the laboratory scale.

Many chemical treatments used to purify other carbon nanomaterials have already been applied to DNDs to improve their purity. Liquid-based purification methods use chromic acid, sulfuric acid,[18] HNO_3,[19,20] H_2SO_4,[14] and HF/HNO_3.[14] Many recent approaches use strong complexing agents[18] or microwaves[21] to remove inorganic impurities. Gas-phase methods using ozone[22] or simple thermal oxidation[14,23] have been proposed as well. The effectiveness of these treatments is still debated, and several limitations appear. Indeed, according to Dolmatov *et al.*, nitric acid only removed 10–15 wt% of metallic impurities and only 5–7 wt% of nondiamond carbons.[18] Conversely, the work by Pichot *et al.* showed that a treatment of a soot containing 17 wt% impurities with H_2SO_4 led to residual levels of inorganic impurities in DNDs of approximately 6 wt% and 1 wt% using an HF/HNO_3 mixture.[14] In addition, most of the reagents used to remove impurities from DND samples, such as CrO_3, $K_2Cr_2O_7$, $KMnO_4$, $HClO_4$ and HF, are corrosive, carcinogenic or harmful to the environment. In brief, the existing purifying methods have several limitations. (i) Their implementation involves using toxic chemicals and produces pollutants difficult to neutralize. (ii) The harsh acid and oxidation conditions used forbid good control over the surface chemistry and a high degree of selectivity, often leading to damaged DND structures and lowered properties. (iii) Such approaches fail to eliminate inorganic impurities, like SiO_2, in DNDs as they are stable in acids and under oxidizing atmospheres.

Interestingly, halogen molecules like Cl_2 and F_2, far less investigated for carbon nanomaterial treatment than the above-mentioned oxidants, have shown a high reaction selectivity when studied separately. Such selectivity is highly demanded to overcome the current bottleneck in the field of DND purification. Despite both being halogens, they behave differently towards carbon species having different hybridizations and inorganic impurities. Cl_2, nonreactive towards sp^2 carbon, unlike F_2, has been reported to allow a process of sublimation of metallic impurities by chlorination for the facile and efficient purification of carbon nanotubes (CNTs), without damaging them.[24–28] However, the purification of DNDs by Cl_2 has been overlooked so far. The only work reported on the chlorination of NDs with the aim of eliminating metallic impurities includes only the quantification of Al, Si, Cr, Fe and Cu by X-ray fluorescence spectroscopy and does not provide any analysis on the possible reaction mechanism involved or the effect of the chlorination treatment on the DND's surface, morphology or other properties.[29] In the literature, the fluorination of DND samples occurs between 150 and 470 °C under a mixture of fluorine and hydrogen gases in a 3 : 1 ratio[30,31] or under pure elemental F_2 gas at 350–500 °C for 12 h under isobaric conditions.[11,32–34] The fluorination of DNDs or their reaction with F_2 has been used for around twenty years to modify their surface chemistry and their optical or electronic properties.[31,35,36] Fluorine shows higher reactivity towards sp^2-hybridized carbons compared to sp^3-hybridized ones. Purifying DNDs using elemental fluorine, F_2,[11,37] a F_2/H_2 mixture,[31,36] and SF_4 and SF_6 plasma treatments[38] has been reported. Oxygenated groups and C–H bonds are replaced by C–F bonds or CF_2 groups,[39] leading to an increase in the hydrophobicity of the resulting fluorinated NDs and, consequently, a reduction in the adsorption of water molecules. Such fluorine-driven properties have been exploited for the calculation of neutron reflectivity, leading to enhanced properties of these fluorinated NDs.[11,39–42] The impact of the F_2 pressure has not been reported so far. To the best of our knowledge, neither a comparative study on the effect of temperature under a pure F_2 atmosphere nor an *in situ* investigation of the resulting fluoride gases has been reported.

The present work originates from the novel idea to combine the effects of chlorine and fluorine treatments, merging the way the two fields of research on carbon nanomaterials, fluorine chemistry and chlorine chemistry, remain unconnected so far. We anticipate producing highly purified DNDs in a selective manner by following this strategy. Apart from assessing the efficiency, the work conducted here entirely takes into account the lack of knowledge on the mechanisms involved in the chemical reactivity of DNDs towards each of the two halogens used. In the following sections, the fluorination mechanism is comprehensively investigated by a well-controlled and complementary approach (i) to follow both the pressure and temperature of F_2 gas during an FTIR study, (ii) to analyze the gas phases by *in situ* FTIR and (iii) to study the influence of F_2 on the metal impurities in DND samples and on the DND nanoparticles themselves. In addition to the in-depth study on the DND fluorination reaction, chlorination and its combination with fluorination are investigated using a set of complementary characterization techniques, *e.g.*, thermogravimetric analysis (TGA), transmission electron microscopy (TEM), Fourier transform infrared (FTIR) spectroscopy (ATR mode), *in situ* gas-phase analysis by CO adsorption, electron paramagnetic resonance (EPR) spectroscopy, solid-state nuclear magnetic resonance (NMR) spectroscopy and N_2 and H_2O adsorption techniques. The chemical reaction mechanisms for DND reactions with both halogen treatments are proposed. To maximize the purification of DNDs, including the removal of both inorganic and surface impurities (sp^2 layers and functional groups), they are first thermally treated separately under chlorine and fluorine gases. After elucidating the involved chemical mechanisms *via* a robust, comprehensive study, the optimized conditions determined for each treatment are applied to DNDs for the proposed Cl_2/F_2 combined method, leading to the production of highly clean DNDs without any external impurities, regardless of their nature: inorganic, organic or carbon-based.

 This journal is © The Royal Society of Chemistry 2026

Open Access Article. Published on 24 February 2026. Downloaded on 3/17/2026 1:39:49 PM.
This article is licensed under a Creative Commons Attribution 3.0 Unported Licence.

2 Experimental section

2.1 Materials

2.1.1 Detonation nanodiamonds. The DNDs were synthesized using a 60/40 mixture of trinitrotoluene (TNT)/cyclotrimethylenetrinitramine (hexogen or RDX), and washed multiple times with acids, in accordance with the TY 2-037-677-94 technical regulation. The DND sample used was provided by the All-Russian Scientific Research Institute of Experimental Physics, Russian Federal Nuclear Center (RFNC-VNIIF), Snezhinsk, Russia. According to the supplier's information, the as-produced DNDs had a mean diameter of 4–5 nm. The DND sample was used as-received, and no deagglomeration treatment was applied before use.

Sodium hydroxide (VWR international, purity 99%) was used as a neutralizing agent for chlorination experiments.

2.2 Sample preparation

2.2.1 Chlorination. A bottle of gaseous Cl_2 supplied by Air Liquide was used (Cl_2 purity >99.5%, H_2O < 40 ppm, NCl_3 < 20 ppm). The experimental setup, placed under a fume hood, schematized in Fig. 1, consisted of a tubular furnace equipped with a 1 m-long quartz tube (diameter = 30 mm). The DND powder (around 150 mg) was placed in a quartz boat (10 cm long and 1 cm wide), which was placed at the center of this tubular furnace. At its ends, pierced rubber plugs were fixed in order to connect this tube to the gas inlet and to three bottles containing NaOH (17 wt%) arranged in series to neutralize unreacted Cl_2. Between the furnace and these three bottles, a so-called guard bottle (empty) was placed to prevent possible reflux of NaOH into the oven. The bottles were connected to each other by phthalate-free polyvinylchloride (PVC) tubes. Before the experiments, a purge with N_2 (flow rate of 100 mL min^{-1}) was initiated for 30 min in order to replace the air from the atmosphere. Then, the oven was heated (heating rate of 10 °C min^{-1}) to the desired temperature, and this temperature was maintained for 1 h. The sample was then cooled naturally under an N_2 atmosphere (flow rate of 100 mL min^{-1}). The Cl_2 and N_2 flow rates were controlled using BROOKS instrument SLA5800 mass flow meters with a SERV instrumentation model 0151 control interface.

2.2.2 Fluorination. The fluorination reaction occurred at several temperatures (25, 100, 400, 485 and 520 °C) but always with 1 bar of pure elemental fluorine for 12 h. The complete details are described in previous works.[11,32] For the FTIR analysis performed *in situ*, fluorination was performed for 60 min at room temperature (RT), 200, 390 and 520 °C (Fig. 2).

The procedure implemented for pressure measurements during DND fluorination was the following: once primary vacuum was applied (10^{-3} mbar, *i.e.*, −1 bar in relative pressure), the F_2 gas was injected at a gas flux of 150 mL min^{-1}. At the same time, the temperature was increased. Then, the flow of pure fluorine was stopped when a total pressure of 1 bar was reached (returned to 0 bar in relative pressure). The pressure in the reactor was measured from the beginning of the experiment until its stabilization at 520 °C using a dedicated set-up, as described in previous works.[11,32–34]

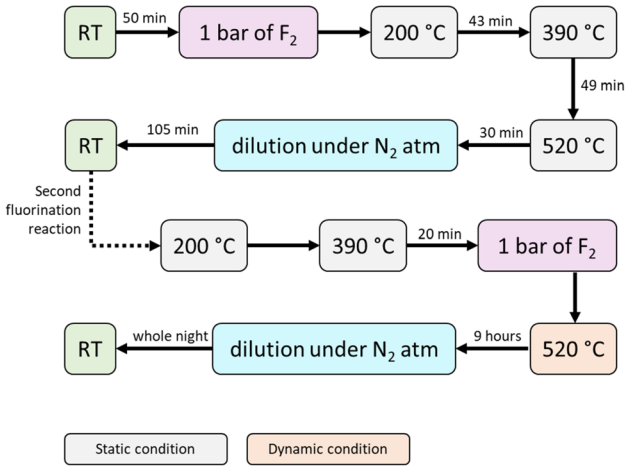

Fig. 2 Flowchart illustrating the fluorination conditions applied to the DND samples for the *in situ* gas-phase experiment. RT stands for room temperature. Different conditions and gases used are represented by different colors: the temperatures used under static conditions (closed reactor) are represented in light grey, and those under dynamic conditions (reactor opened towards the soda lime trap) are represented in orange. N_2 and F_2 gases are represented in blue and pink, respectively.

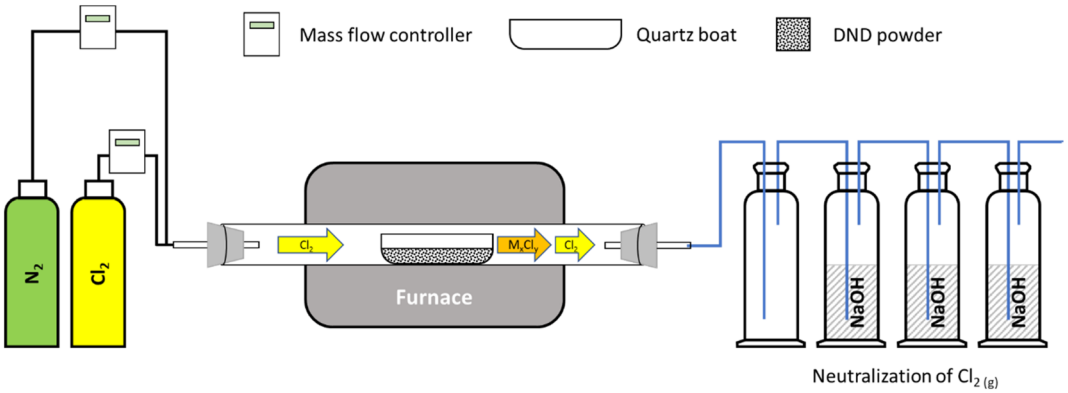

Fig. 1 Scheme of the set-up used for the chlorination treatments applied to DNDs.

Open Access Article. Published on 24 February 2026. Downloaded on 3/17/2026 1:39:49 PM.
This article is licensed under a Creative Commons Attribution 3.0 Unported Licence.

Table 1 lists the samples studied with the applied treatments and the experimental conditions used.

2.3 Characterization

TGA analysis was performed with a Setaram Setsys Evolution 1750. The raw or treated DND powder (around 20 mg) was placed in an alumina crucible and transferred to the TGA chamber, which was first purged of the atmospheric air using a dry air stream (flow rate = 20 mL min^{-1}) for 1 h. The temperature program consisted of heating from room temperature (RT) to 900 °C at 5 °C min^{-1} under an air flow rate of 20 mL min^{-1}, followed by cooling at 20 °C min^{-1} under the same flow rate. Under the used conditions, the precision of the TGA measurements determined from repeatability tests was ±0.8 wt%.

Nitrogen adsorption isotherms were measured at −196 °C (77 K) using a Micromeritics ASAP 2020 automatic apparatus. Before measurements, DND and F-DND samples were pretreated under a secondary vacuum at 150 °C for 3 h for sufficient removal of adsorbed impurities. A second outgassing step was done for 2 h at the analysis port after free-space calibration with He.

Water adsorption/desorption isotherms were measured at 25 °C using the same equipment, with 90 °C for 1 h and 150 °C for 3 h as the degassing conditions.

2.3.1 CO adsorption followed by infrared spectroscopy. DNDs and F-520-DND were first pelletized using a hydraulic press (1–2 ton pressure). The 10–60 mg pellets were then placed in an IR cell and fitted with a quartz or CaF_2 window. They were pre-treated *in situ* overnight at 300 °C under a nitrogen flow (approx. 100 mL min^{-1}). The cell was cooled to −173.15 °C (100 K) with liquid nitrogen, and a reference spectrum was recorded using a Nicolet iS50 spectrometer. CO doses of a fixed volume (V = 0.4125 cm^3) were injected at a known CO pressure (from 5 to 200 mbar) until saturation, which was obtained by subjecting the samples to a CO pressure of 1 mbar at equilibrium. After the introduction of each dose, an IR spectrum was recorded for wavenumbers between 1100 and 4000 cm^{-1} with a resolution of 4 cm^{-1} and 64 scans. Each spectrum was then subtracted from the reference spectrum and normalized to a sample mass of 25 mg.

Transmission electron microscopy (TEM) was performed with a JEOL JEM-ARM 200F Cold FEG apparatus equipped with a spherical aberration (C_s) corrector working at an accelerating voltage of 200 kV. High-angle annular dark-field (HAADF) and bright-field (BF) images were obtained in the scanning transmission electron microscopy (STEM) mode. X-maps were recorded on a JEOL spectrometer (SDD, JEOL DRY SD 30 GV).

Electron paramagnetic resonance (EPR) spectroscopy was carried out using an X-band Bruker EMX spectrometer operating at 9.85 GHz. Spectra were recorded at room temperature under air and vacuum with a 21.73 mW microwave power after checking the linearity of the intensity/square root of the power curve in the 0.22–108.9 mW range to check the nonsaturation regardless of the power. Only the relative changes in the spin densities were discussed by comparison with the raw DNDs. To this end, integrated signals were considered.

2.3.2 Infrared spectroscopy. An FTIR spectrometer, NICOLET 5700 (thermo electron), was used to record IR spectra in both ATR and transmission modes. The IR spectra were collected between 4000 and 400 cm^{-1} with a 4 cm^{-1} resolution and 100 scans. The single-reflection ATR accessory (Thermo

Table 1 List of the treated samples along with the experimental conditions used and their corresponding name. For all the treatments under chlorine, the Cl_2 flow rate was 20 mL min^{-1}, and the treatment duration was 1 h. For all the treatments under air, a pump was used to continuously supply the system with air. For all the treatments under fluorine, the pressure was 1 bar, and the treatment duration was 12 h

		Chemical treatment and experimental conditions	
Treatment nature	Sample name	First treatment	Second treatment
Chlorination	Cl-500-DND	Cl_2, 500 °C	No
	Cl-600-DND	Cl_2, 600 °C	No
	Cl-650-DND	Cl_2, 650 °C	No
	Cl-700-DND	Cl_2, 700 °C	No
	Cl-800-DND	Cl_2, 800 °C	No
	Cl-900-DND	Cl_2, 900 °C	No
Oxidation	O-DND	Air, 600 °C	No
Chlorination and oxidation	O-Cl-650-DND	Cl_2, 650 °C	Air, 600 °C
	O-Cl-700-DND	Cl_2, 700 °C	Air, 600 °C
	O-Cl-800-DND	Cl_2, 800 °C	Air, 600 °C
	O-Cl-900-DND	Cl_2, 900 °C	Air, 600 °C
Fluorination	F-RT-DND	F_2, RT	No
	F-RTx2-DND	F_2, RT	F_2, RT
	F-100-DND	F_2, 100 °C	No
	F-100x2-DND	F_2, 100 °C	F_2, 100 °C
	F-400-DND	F_2, 400 °C	No
	F-485-DND	F_2, 485 °C	No
	F-520-DND	F_2, 520 °C	No
Fluorination and oxidation	O–F-520-DND	F_2, 520 °C	Air, 600 °C
Chlorination and fluorination	F-Cl-DND	Cl_2, 650 °C	F_2, 520 °C

 This journal is © The Royal Society of Chemistry 2026

Open Access Article. Published on 24 February 2026. Downloaded on 3/17/2026 1:39:49 PM.
This article is licensed under a Creative Commons Attribution 3.0 Unported Licence.

Scientific Smart Orbit) operated with a durable diamond crystal (type IIa diamond tungsten carbide mounted in stainless steel with a refractive index of 2.4 and an incident angle of 58°) and a swivel pressure tower that ensured consistent pressure from one sample to the other sample. The active sample area was 1.5 mm^2. A wide spectral range (10 000 to below 200 cm^{-1}) and a good depth of penetration (DP of 2.03 μm at 1000 cm^{-1}) were then reached. In-line infrared spectra were collected during the fluorination of DNDs using a Nicolet Summit FTIR spectrometer (Thermo Scientific) equipped with a MercuryTM gas cell (10 cm cell path and CaF_2 windows) coupled with a passivated nickel reactor. Spectra were recorded in the 1000–4000 cm^{-1} range with a 4 cm^{-1} resolution and 16 scans.

Solid-state nuclear magnetic resonance (NMR) experiments were carried out using a Bruker Avance spectrometer at operating frequencies of 300.1, 282.2 and 75.4 MHz for ^1H, ^{19}F and ^{13}C nuclei, respectively. A simple sequence (τ-acquisition) was used with a single π/2 pulse length of 3.5 μs for ^1H and ^{13}C nuclei with magic angle spinning (MAS) and recycle times of 5 and 25 s, respectively. For ^{19}F MAS spectra, the π/2 pulse duration was 5.5 μs, and the recycle time was equal to 3 s. $^1H \rightarrow {}^{13}C$ and $^{19}F \rightarrow {}^{13}C$ cross-polarization (CP) spectra were also measured when ^1H and ^{19}F nuclei were present in significant amounts. ^{19}F chemical shifts were referenced to $CFCl_3$. Tetramethylsilane (TMS) was the reference for both ^1H and ^{13}C chemical shifts. The fits were performed using Lorentzian functions on the origin software.

3 Results

As previously mentioned, DND samples contain various kinds of impurities. Except for low-density paramagnetic internal defects, which can be valuable for specific properties, most of them are located outside and on the surface of the nanodiamond particles. In this work, raw DNDs, naturally in the form of agglomerates or chaplets several hundred nanometers in size,[13] were thermally treated under chlorine or/and fluorine gas without performing any prior deagglomeration process. The purification approach is based on a two-step halogen-based sequential process aimed at removing all the external and surface impurities present in DNDs. In the following sections, the experimental conditions are optimized thanks to in-depth structural and chemical investigations of the treated DNDs after undergoing each of the halogen-based chemical treatments.

3.1 Quasi-complete elimination of inorganic impurities from DNDs by chlorine

To achieve an high purification yield of DNDs by chlorine treatment, three experimental parameters were optimized: the duration of chlorination, the flow rate of chlorine and the temperature at which the sample was remained under the chlorine stream. For the sake of clarity, the optimizations of the duration and flow rate of chlorine are described in the SI, Fig. S1 and S2, respectively. The best conditions found are a chlorine flow rate of 20 mL min^{-1} and a duration of 1 h. In the following experiments, keeping these two conditions fixed, the impact of temperature (varied from 500 to 900 °C) on the Cl_2-based purification efficiency is investigated by TGA and FTIR analyses.

The thermogram profiles of carbon nanomaterials from TGA under air are commonly used to assess the efficiency of purification methods. Two different parameters can be analyzed: (i) the remaining nonburnt inorganic residues to minimize and (ii) the combustion temperature of the carbon species to maximize. Indeed, the metallic-based impurities have catalytic properties towards the combustion of carbon materials, and their removal leads to a stabilization of the purified materials against oxidation, which means that their combustion temperature increases.[24,26] Fig. 3a shows the thermograms of the raw DND sample and the DND samples treated with chlorine at 500, 600, 650, 700, 800 and 900 °C for 1 h (with a Cl_2 flow rate of 20 mL min^{-1}). For the raw DND sample, a dehydration phenomenon leading to a slight decrease in the weight is observed at around 100 °C (inset, Fig. 3a). An increase in the mass is observed from 300 to 425 °C, corresponding to the oxidation of the metal-based impurities. Neither dehydration nor metal oxidation is observed for the treated DND samples. In the 450–600 °C range, the weight of all samples strongly decreases due to the burn off of the DNDs. For the raw DNDs, the remaining weight is 3.5 ± 0.8 wt% of residues. After treatment at temperatures higher than 500 °C, the residue content decreases to around 1 wt%; it is 2.4 ± 0.8 wt% for Cl-500-DND (Fig. 3b and its inset). After treatment with Cl_2, the content of inorganic impurities significantly reduces, and it falls below the limit of detection (LOD) of TGA (typically below 1.5–1.0 wt%), which forbids the purification assessment for parameter *i*.[43]

Regarding the second parameter (ii), the combustion temperature of the Cl_2-treated DNDs gradually upshifts with an increase in the treatment temperature (Fig. 3a–c). The thermograms of all treated samples show two different combustion rates: a rapid phenomenon noticeable by a sharp peak and a much slower one exhibiting a broader signal in the derivative representation (Fig. 3c). For the purpose of clarifying the mechanisms involved in the thermal treatment of DNDs under dry air, the shape of DND thermograms was modeled by the four behaviors possibly observable for DNDs heated under dry air by TGA: dehydration, metal oxidation, and rapid and slow combustion processes (SI, Fig. S3). From this analysis, it is evident that these two combustion processes behave independently. The temperature of the rapid combustion is upshifted from 485 to 599 °C when DNDs are treated under Cl_2 from 500 to 900 °C. The slow combustion temperature upshifts and reaches around 550 °C for Cl-650-DND as the chlorination temperature increases from 500 to 900 °C. Obviously, the temperature used for the treatment under chlorine has a greater impact on the rapid combustion process. Such rapid combustion of DNDs during TGA measurements has already been observed in the reported thermograms of DNDs; unfortunately, it has not been discussed or analyzed.[44] The proportion of the DND sample affected by this rapid combustion is very small, around 2 wt%, regardless of the sample (raw or treated) used. The corresponding carbonaceous species are probably thin sp^2 carbon layers surrounding the diamond core of DNDs, which undergoes a graphitization

Open Access Article. Published on 24 February 2026. Downloaded on 3/17/2026 1:39:49 PM.
This article is licensed under a Creative Commons Attribution 3.0 Unported Licence.

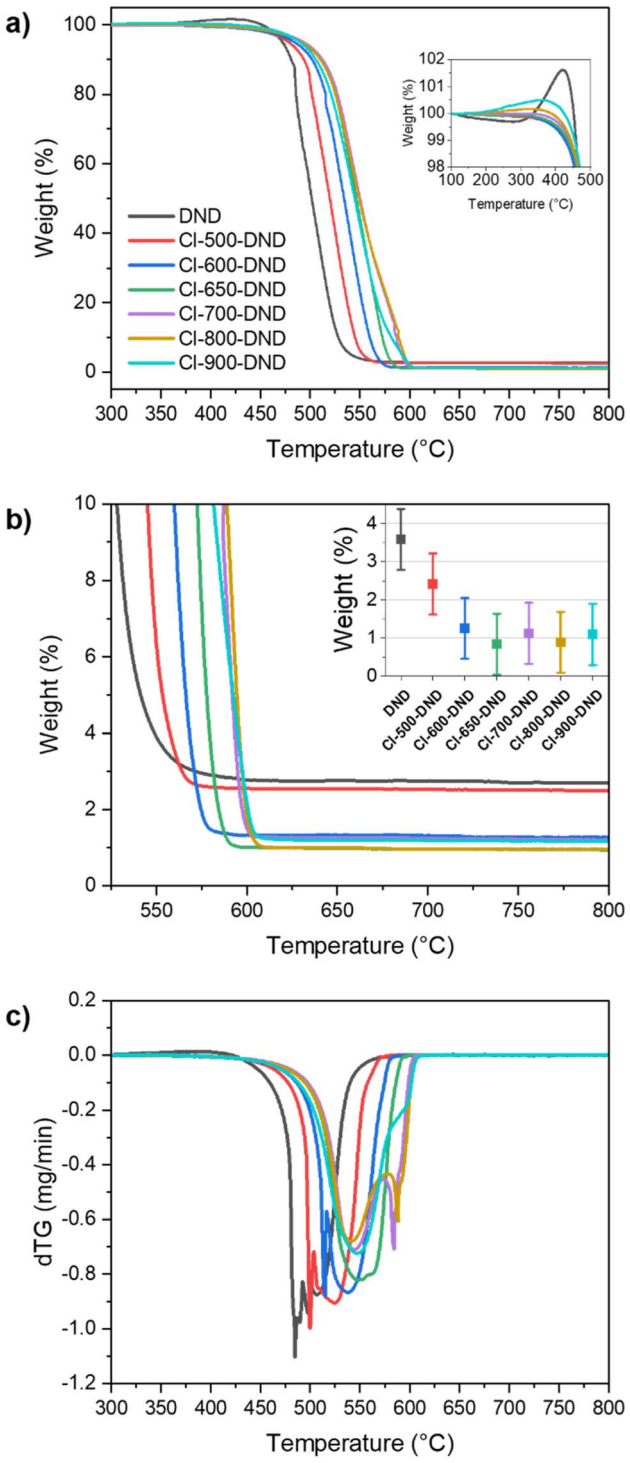

Fig. 3 (a) Thermograms under dry air of raw DNDs and DNDs treated under a Cl_2 atmosphere for 1 h at 20 mL min^{-1} from 500 to 900 °C; (inset) Zoomed-in image of the low-weight variation domain. (b) Zoomed-in image of the thermograms in the high-temperature domain; (inset) Remaining weights after DND combustion. (c) dTG representation of the thermograms in (a).

process with a rise in the treatment temperature, inducing its stabilization under air and the observed upshift of its combustion temperature. The main part of the raw and chlorine-treated DND samples burns off at a slower rate.

FTIR spectroscopy is another commonly used technique to assess the efficiency of purification.[45] Here, FTIR is particularly powerful because it is sensitive to both inorganic and carbon species. Prior to the FTIR analysis, the inorganic impurities were concentrated by performing a selective combustion of the treated DND samples using a simple method developed previously.[13] From the FTIR spectrum of the resulting ashes of the raw DND sample (O-DND), Si, Cr and Fe are identified as the main impurities in the raw DNDs, which are present in the form of silicon oxide (SiO_2) and a mixture of pristine chromium(III) oxide (Cr_2O_3) and a solid solution of $Cr_{2-x}Fe_xO_3$ (Fig. 4a). The FTIR spectra of the oxidized Cl_2-treated DND samples (O-Cl-DND series) after chlorination in the 650–900 °C range show a drastic decrease in the intensity of both chromium- and iron-based impurities. Only the vibrations assigned to silicon oxide are still detected without a significant difference in intensity, regardless of the temperature used for the DND treatment under Cl_2. No other metal-based (oxide or chloride) or inorganic compounds are noticeable in the FTIR spectra of the O-Cl-DND series.

The effect of the chlorine treatment on the functional groups present on the DND surface was also investigated. Fig. 4b shows the FTIR spectra of DNDs before and after chlorination. The FTIR spectra of the Cl_2-treated DNDs are quite similar, regardless of the chlorination temperature, but they are drastically different from those of the original DNDs. In the 900–1400 cm^{-1} range, the features of the Cl_2-treated DNDs are broader than those of the as-received sample, and two new bands appear at 1200 and 1273 cm^{-1}. They are attributable to N-based bonds,[46] which become detectable after the purification treatment. In the low-wavelength spectral region, below 800 cm^{-1}, the FTIR spectra appear much more flattened after chlorination. The vibrations of –OH (2900–3500 cm^{-1}) and –CH (2850 and 2950 cm^{-1}), clearly noticeable for the raw DNDs, are not detected for the Cl-DND series anymore. The presence of very weak C–H and OH bands in the spectra of Cl-650-DND and Cl-900-DND is due to the ethanol used to clean the spectrometer. The peaks of carbonyl (C=O) and ether (C–O–C) functional groups are also observed around 1730 cm^{-1} and in the 1000–1200 cm^{-1} spectral range, respectively.

To summarize, the Cl_2 treatment allows the removal of hydrogenated and hydroxyl functional groups from DNDs, providing evidence of the efficient surface cleaning by heating the sample under Cl_2 in the temperature range used. Moreover, heating DNDs under chlorine at 650 °C and a Cl_2 flow rate of 20 mL min^{-1} for 1 h creates the best experimental conditions, resulting in the highest purification efficiency, as evidenced by both TGA (showing a combustion temperature upshift of around 50 °C) and FTIR (showing that only SiO_2 remains in Cl-650-DND, and all other functional groups and inorganic impurities are removed by chlorination).

3.2 Clarifying the chemical mechanisms involved in the fluorination of DNDs

3.2.1 Unveiling anomalous behavior of F_2 pressure during the fluorination of DNDs towards the elimination of various types of DND impurities. Regarding the reactivity of DNDs with

Open Access Article. Published on 24 February 2026. Downloaded on 3/17/2026 1:39:49 PM.
This article is licensed under a Creative Commons Attribution 3.0 Unported Licence.

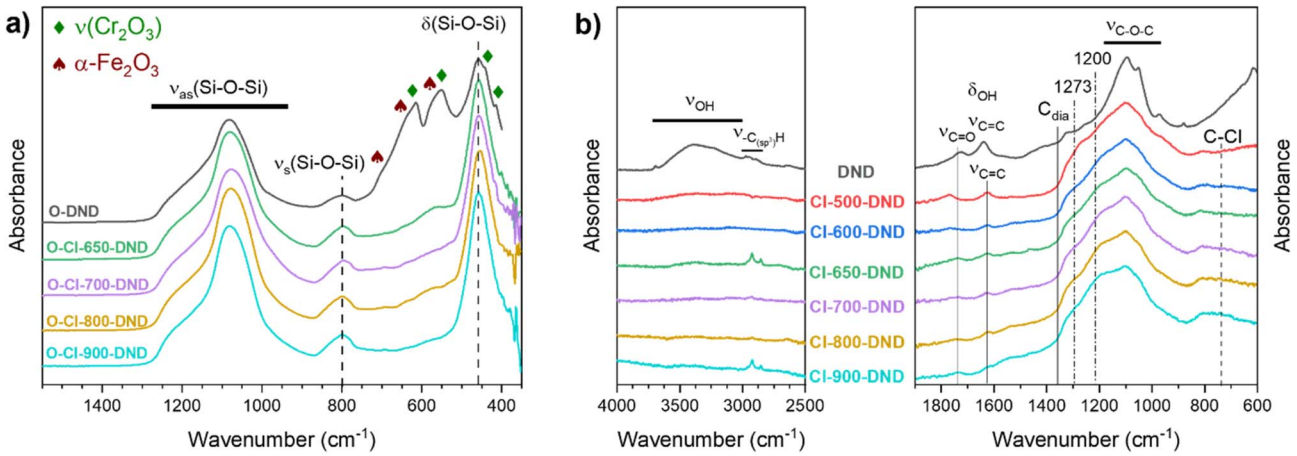

Fig. 4 (a) FTIR spectra of the raw and chlorinated DNDs after their selective combustion by the SC-DND method. The samples are named O-DND for the ashes of raw DNDs and O-Cl-650-DND, O-Cl-700-DND, O-Cl-800-DND and O-Cl-900-DND for the ashes of the DND samples treated under Cl_2 at 650, 700, 800, and 900 °C (Cl-DND series), respectively. Cr_2O_3 and α-Fe_2O_3 species are represented by green diamonds and brown spades, respectively. (b) FTIR spectra of the DND and Cl-DND series at temperatures ranging from 500 to 900 °C.

F_2, the sp^3-hybridized carbon atoms in DNDs are expected to react poorly with F_2. Conversely, if they bear defects, the chemical reactivity of F_2 toward the disordered sp^2 shells surrounding the DND's diamond core is expected to be much more favored.[47] The FTIR features of DNDs after a fluorination treatment at temperatures ranging from RT to 520 °C are strongly altered even when the reaction with F_2 occurs at RT (Fig. 5a), providing evidence of the high reactivity of the DND surface toward F_2 and its exothermic character (SI, Fig. S4). At high wavenumbers, the bands of hydroxyl functional groups (3000–3600 cm^{-1}) disappear, providing evidence that these groups are clearly removed from the DND surface, similar to that observed for the chlorinated DNDs. In the 800–2000 cm^{-1} range, the band of sp^3 C from the C–C bonds of the diamond type (1344 cm^{-1}), *i.e.,* of the diamond core, is much more pronounced for all the fluorinated DNDs.

In the low-fluorination-temperature range, at RT and 100 °C, the samples underwent either one (F-RT-DND and F-100-DND) or two successive reactions with F_2 (F-RTx2-DND and F-100x2-DND). These two successive fluorinations guarantee the completion of the reaction. For all these low-temperature fluorinated DNDs, two sharp vibration bands of C–F bonds appear, assigned to $C_xF_{y(s)}$ groups at 1244 and 1220 cm^{-1} from the fluorine grafted onto the sp^2 DND shell. These $C_xF_{y(s)}$ groups have to be differentiated from the F grafted on the diamond core, referred to as C–F. Additional bands at 992 and 963 cm^{-1} are also observed for F-RTx2-DND, F-100-DND and F-100x2-DND. According to the literature, $-CF_3$ and $-CF_2$ bands from linear fluorocarbons are localized in the 1235–1250 cm^{-1} [48–50] and 1220–1225 cm^{-1} ranges,[48–52] respectively. The vibration bands of C–C bonds belonging to the cyclic backbone of fluorocarbons (ring motions) are expected in the 850–1000 cm^{-1} range, even though some linear conformers of fluorocarbon compounds can also exhibit coupled C–C/C–F vibration modes around 850–1000 cm^{-1}.[53,54] Consequently, the observed vibrations attributed to $C_xF_{y(s)}$ compounds are related to $-CF_3$ (1244 cm^{-1}) and $-CF_2$ (1220 cm^{-1}) groups of linear fluorocarbons, while the bands at 992 and 963 cm^{-1} indicate the presence of cyclic fluorocarbon species at low fluorination temperatures.

Interestingly, when the fluorination reaction is conducted at a much higher temperature (>400 °C), the vibration bands of $C_xF_{y(s)}$ are no longer observed in the FTIR spectra of F-DND samples. This implies that these compounds are totally volatilized as gaseous species during the fluorination. The addition of F_2 molecules to the $C_xF_{y(s)}$ species results in their decomposition when fluorination occurs in the high-temperature domain, typically higher than 400 °C.

With the aim of elucidating the origin of the observed strong modification of the surface chemistry of DND through fluorination when the temperature increases, the pressure was measured during the reaction of DNDs with F_2 in a closed reactor as a function of time with increasing temperature from RT to 520 °C (Fig. 5b). For this experiment, after air pumping until −1 bar (relative pressure) to remove air and moisture after reactor closure, F_2 was injected into the closed reactor, where the raw DND powder was placed, to reach 1 bar of F_2 inside the reactor (corresponding to 0 bar in Fig. 5b). This F_2 introduction induces the expected gradual increase in pressure in the reactor until around 840 s (14 min). During this step, the temperature is 350 °C. The shutting down of F_2 injection is visualized on the curve by an expected decrease in pressure and a plateau. A few minutes later (at 400 °C, 1000 s), because the temperature is still increasing, the pressure increases as well (due to the ideal gas law). At around 485 °C, the pressure drops suddenly and significantly to around 0.2 bar (1345 s). Next, the F_2 pressure increases slowly and stabilizes at around 4000 s when the temperature has reached 520 °C and the fluorination is completed.

The reaction was completely stopped at different stages/temperatures of interest during the reaction of DNDs under fluorine in the high-temperature domain (400–520 °C) to

Open Access Article. Published on 24 February 2026. Downloaded on 3/17/2026 1:39:49 PM.
This article is licensed under a Creative Commons Attribution 3.0 Unported Licence.

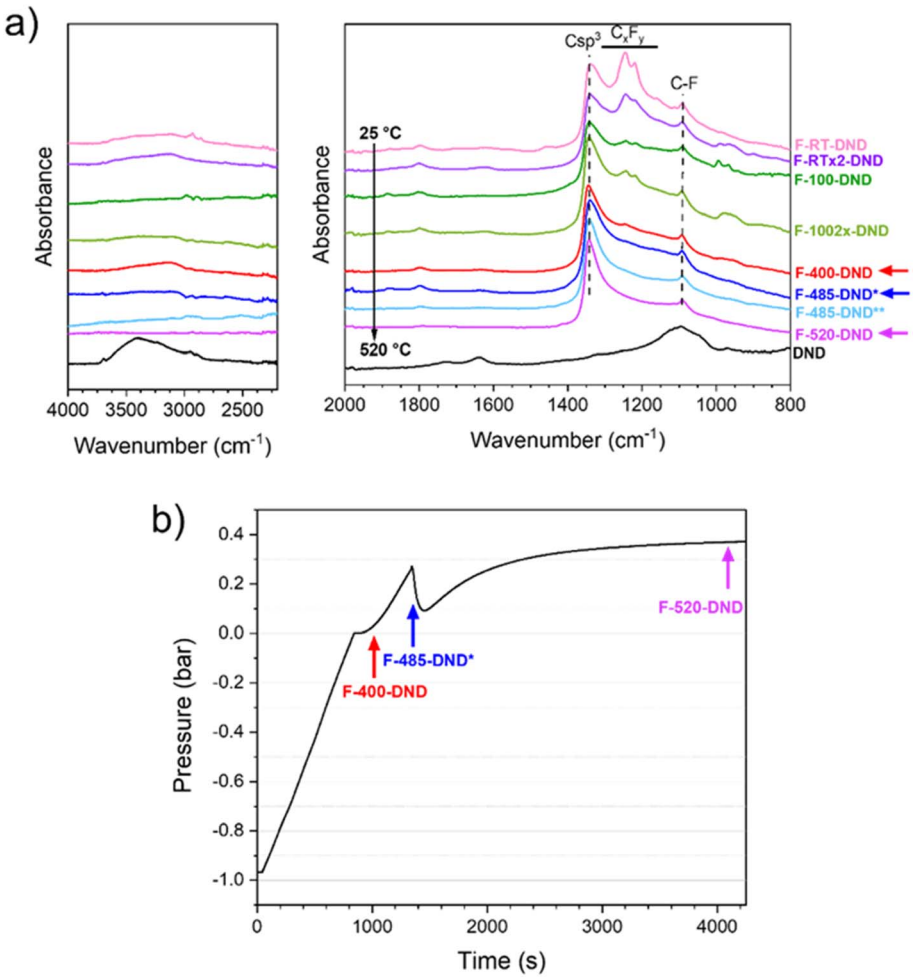

Fig. 5 (a) FTIR spectra of DNDs fluorinated at temperatures ranging from RT to 520 °C. (b) Fluorine pressure (in bar) represented as a function of time (in seconds). For visibility purposes, the samples F-400-DND, F-485-DND and F-520-DND are represented by red, blue and pink arrows, respectively, in both panels.

prepare (i) F-400-DND at 400 °C; (ii) other samples (F-485-DND* and F-485-DND**) separated in two parts (corresponding to two slightly different colors noticed by the naked eye) of DNDs fluorinated at 485 °C, prepared by fluorination at a temperature as close as possible to the anomalous pressure event noticed at around 485 °C; and (iii) F-520-DND fluorinated at 520 °C. The corresponding FTIR spectra (Fig. 5a) show the vibrations of $C_xF_{y(s)}$ compounds around 1230 cm^{-1} when the fluorination temperature is below 485 °C (with a very weak intensity at 400 °C), while above 485 °C, $C_xF_{y(s)}$ are no longer present, indicating their complete elimination from the F-DND surface.

The conducted *ex situ* FTIR investigation, combined with the pressure measurements when the temperature increases during the fluorination of the DND powder, allows us to propose the following fluorination mechanism: (i) in a quite low temperature range, including RT, DNDs and especially their surrounding sp^2 shells are expected to be very reactive towards fluorine. The F_2 consumed by the fluorination reaction is balanced by F_2 gas introduction, leading to the observed pressure increase at the beginning of the reaction. When the F_2 injection is stopped, the rise in pressure slows down. (ii) When the temperature reaches 485 °C, fluorocarbon species on the DND surface are completely decomposed. This process suddenly leads to a new cleaned and fresh DND surface that is accessible for reaction with F_2 molecules, allowing further covalent grafting of fluorine over a short period of time. The resulting rapid impoverishment of F_2 in the reactor may be the cause of the observed drop in pressure and the anomalous pressure event revealed here. (iii) As the temperature rises further, the release of the newly formed fluorocarbons induces the observed increase in pressure inside the reactor until its stabilization once the DND surface is stabilized with only C–F bonds.

Complementary to the *ex situ* FTIR study of the fluorinated DNDs described above, with the aim of identifying the nature of the fluorocarbon species (C_xF_y) formed during fluorination, *in situ* FTIR analysis of the gas emitted during the fluorination reaction was conducted under different conditions. The FTIR spectrum of the fluorination reaction performed at RT after 50 minutes is shown in Fig. 6 (time-resolved FTIR spectra are

 This journal is © The Royal Society of Chemistry 2026

Open Access Article. Published on 24 February 2026. Downloaded on 3/17/2026 1:39:49 PM.
This article is licensed under a Creative Commons Attribution 3.0 Unported Licence.

shown in SI, Fig. S5). Other experimental conditions were also investigated, including (i) a temperature increase from 200 to 520 °C in static mode and (ii) heating at 200 and 390 °C under static conditions, followed by heating at 520 °C under dynamic conditions (SI, Fig. S6). The FTIR spectrum of the emitted gas after 50 min of the reaction between F_2 and DNDs at RT shows the presence of numerous species (Fig. 6a). For the sake of clarity, the complete FTIR spectrum is displayed as three magnified parts (Fig. 6b–d).

In the highest spectral domain (Fig. 6b), the two observed series of vibration bands around 3960 cm^{-1} are typical of the rotational transitions of hydrogen fluoride, HF.[55,56] HF is probably formed from the reaction between hydrogen-containing functions and F_2. The detected HF positions are listed in SI, Table S1, in full agreement with the literature.[55,56] The vibrational bands of CO_2 are observed alongside the HF peaks, for CO_2 combination bands ($\nu_1 + \nu_3$) at 3728 and 3704 cm^{-1} and ($2\nu_2 + \nu_3$) at 3626 and 3601 cm^{-1}.[57–59] Only ν_3 is visible in Fig. 6c because ν_1 is infrared inactive, and ν_2 is located below 900 cm^{-1}. During fluorination, the release of CO_2 adsorbed onto and within the sp^2 layers surrounding the diamond core is favored by $C_xF_{y(s)}$ formation because the sp^2 layers are consumed. CO_2 probably produces COF_2 by interacting with F_2 because its absorption bands are detected at 1956, 1928, 1252 and 1235 cm^{-1}.[60–62] Moreover, as discussed above, $C_xF_{y(s)}$ tend to detach from DND and form diverse fluorocarbons $C_xF_{y(g)}$ whose presence in the vicinity of DNDs can be detected by FTIR (Fig. 6c and d): vibrations of CF_4,[48,63] C_2F_6 (refs. 48 and 63) and C_4F_{10}.[48,64] A majority of these fluorocarbons lead to strong vibrations in the range of 1000–1400 cm^{-1}.[48,64]

The release of silicon fluoride compounds is also detected (Fig. 6c), particularly SiF_4 (1028 cm^{-1}), SiF_3H (1005 and 990 cm^{-1}) and SiF_3CH_3 (981 cm^{-1}).[65–67] The favored removal of SiO_2 from DNDs by elemental fluorine, even at RT, is clearly demonstrated here, in agreement with the widely known reactivity of HF or F_2 with glass and silica. The release of fluorocarbons (CF_4, C_2F_6, and C_4F_{10}), hydrogen, carbonyl and silicon fluoride (HF, COF_2 and SiF_4, respectively), and fluorosilanes

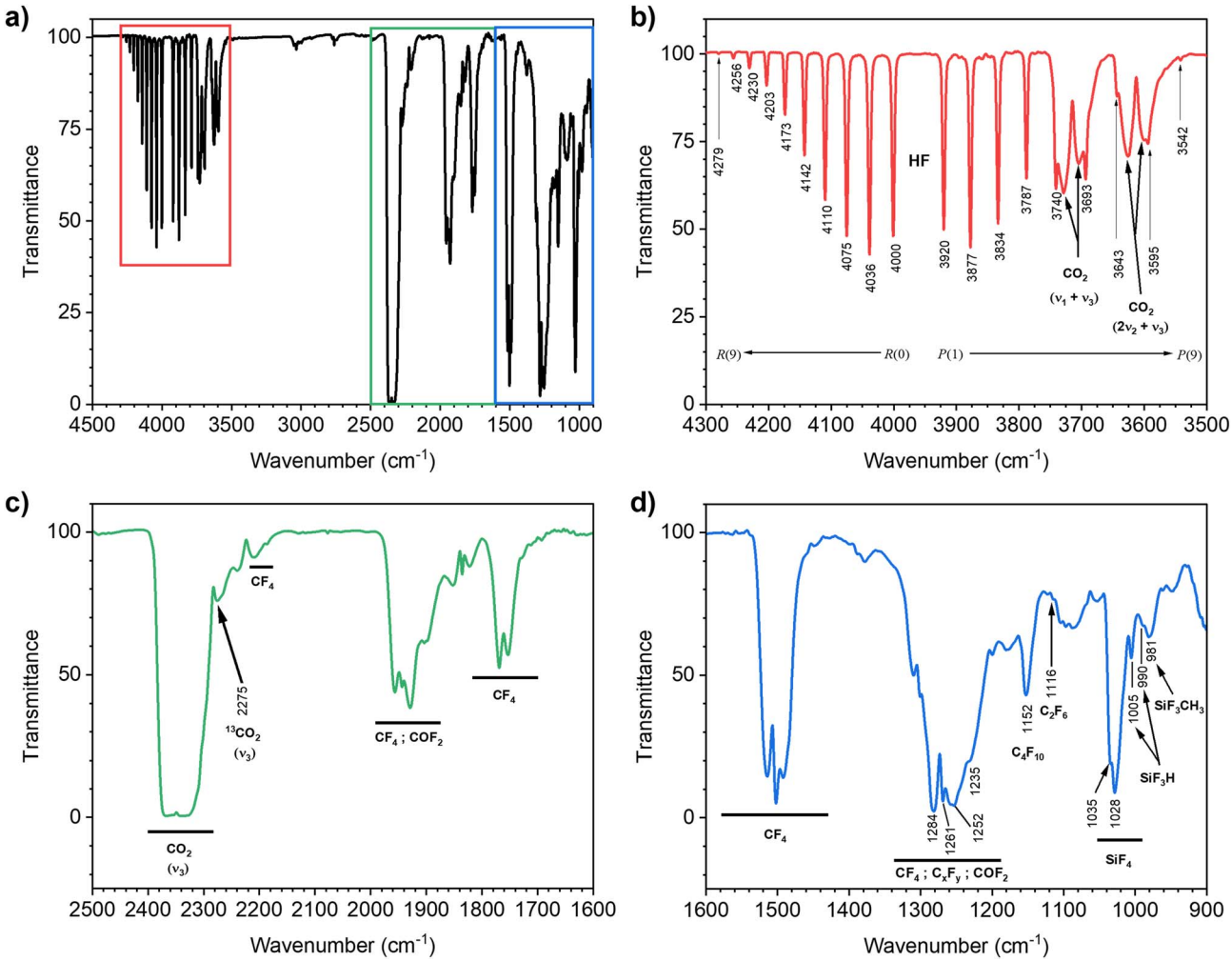

Fig. 6 (a) *In situ* gas phase FTIR spectrum of DND after 50 min of fluorination at RT. The spectrum is divided into three magnified parts for the sake of clarity: (b) from 4300 to 3500 cm^{-1}, (c) from 2500 to 1600 cm^{-1} and (d) from 1600 to 900 cm^{-1}, represented in red, green and blue, respectively.

Open Access Article. Published on 24 February 2026. Downloaded on 3/17/2026 1:39:49 PM.
This article is licensed under a Creative Commons Attribution 3.0 Unported Licence.

(SiF_3H and SiF_3CH_3) is in agreement with additional experiments performed at higher temperatures under both static and dynamic conditions (SI, Fig. S5 and S6).

3.2.2 Effect of fluorine treatment on paramagnetic centers present in DNDs. With the objective of providing a comprehensive study on DND purification, and even though the paramagnetic centers (PCs) located in the DND core are not accessible to chemical treatments, they were also studied in this work by EPR and IR spectroscopy. Based on the literature on the analysis of DNDs, EPR is a powerful technique to discriminate between the location of the PCs because it is sensitive to the local order of materials (SI, Section 2.3). The EPR spectra of raw DNDs and F-520-DND (fluorination at 520 °C, optimized conditions) were recorded in air and under primary vacuum (10^{-3} mbar) (Fig. 7a). They both adopt a typical quasi-Lorentzian profile with a *g*-factor of 2.004 (3450 G) from the so-called N_0 (P_1) or dangling bonds (DBs), where a *g*-factor of 2.003 is expected.[68,69] When O_2 is present in its surrounding medium, the EPR signal of the fluorinated DNDs is only slightly modified, whereas that of raw DNDs is significantly decreased to 21% (the straight line in Fig. 7a; see also the inset showing the integrated area of the signals). Paramagnetic O_2 molecules quench the signal of PCs close to the surface, *i.e.*, at a distance for O_2-PC magnetic interactions. The percentage of loss when the spectrum is recorded in air can be used to directly quantify the percentage of PCs located close to the surface, *i.e.*, 21% in raw DNDs. The efficient removal of PCs close to the surface by fluorination is responsible for its non-sensitivity towards the surrounding medium.

The peak-to-peak linewidth, ΔH_{pp}, of the F-520-DND signal is lower than that of the raw DNDs (Fig. 7b). The modification of the surrounding medium has a significant impact on the ΔH_{pp} of the raw DNDs, which is 0.1 G wider from vacuum (dotted line) to air (straight line), while that of the fluorinated DNDs is hardly affected by the medium change. The observed broadening of the EPR spectrum is attributed to the presence of sp^2-hybridized carbons because the hyperfine coupling with ^{19}F nuclei (I = 1/2) results in an unresolved hyperfine broadening.

In order to confirm the removal of surface structural defects, raw and fluorinated DND (F-520-DND) samples were studied by CO adsorption, followed by infrared, which is usually used as a probe molecule to characterize acidic properties (Brønsted and Lewis). CO adsorption can be characterized by various bands, respectively, between 2160 and 2240 cm^{-1} for Lewis acidity and in the range of 2150–2180 m^{-1} for Brønsted acidity [5, 11]. Fig. 7c displays the FTIR spectra of DND and F-520-DND after CO adsorption. The DND spectrum (black line) shows bands at 2185 cm^{-1}, around 2165 cm^{-1} and at 2151 cm^{-1}, corresponding to coordinatively unsaturated sites (cus) with various strengths of Lewis acidity. Because diamond is composed of saturated carbons in an sp^3-hybridized state, the observed CO bands can be attributed to unsaturated sp^2-hybridized carbons (with unoccupied 2p orbitals) that exist in different configurations or chemical environments. The band at 2185 cm^{-1} can be attributed to the higher strength of Lewis acidity, followed by a site of middle strength at 2165 cm^{-1} and the lowest one at 2151 cm^{-1}. The shoulder in the 2115–2135 cm^{-1} range corresponds to physical CO adsorption.[70,71] Because surface hydroxyl groups were detected earlier by IR spectroscopy (see Fig. 5a), the 2150 cm^{-1} band may also correspond to CO···OH interactions, as described in the literature.[71–76] Hence, this band can be ascribed to a CO adsorption site with a low-to-medium acidic strength close to hydroxyl groups.

After fluorination (F-520-DND), the band intensity of the Lewis strength region (2150–2200 cm^{-1}) decreases strongly compared to the non-fluorinated sample, corresponding to the disappearance of CO adsorption (cus ions or electronic deficiencies) due to fluorine grafting. This phenomenon is similar to the disappearance of DB and PC on the F-520-DND surface observed in the EPR spectrum (Fig. 7a). It has been shown[77,78] that surface-fluorinated catalysts, compared to oxides, exhibit (i) a higher frequency of CO bands due to the inductive effects of the fluorinated environment (higher electronegative ions) and (ii) a decrease in band intensity, corresponding to the elimination of the acid sites. At first sight, no increase in the frequency is noted after the fluorination treatment of DNDs.

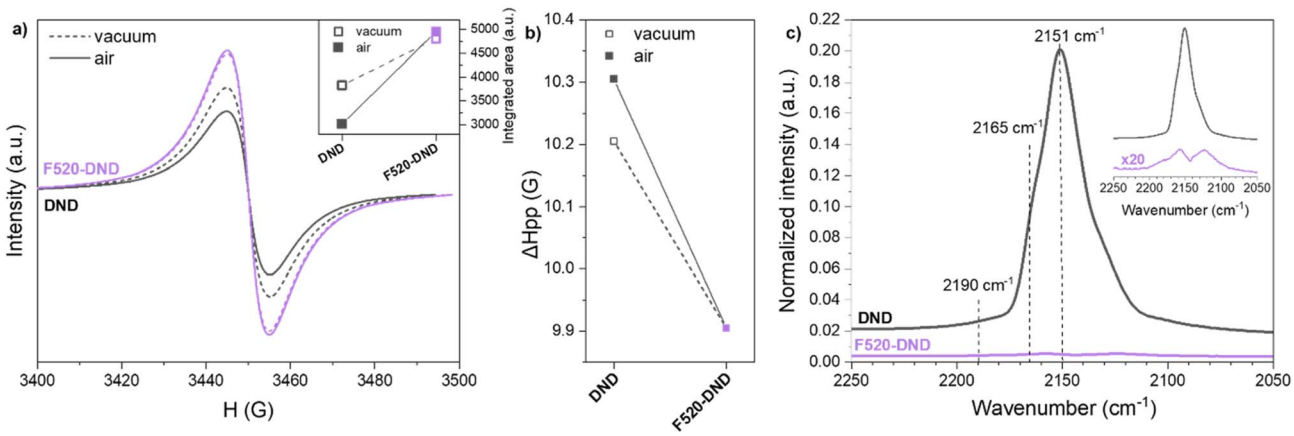

Fig. 7 (a) EPR spectra and integrated areas (inset) of DNDs and F-520-DND and (b) the peak-to-peak linewidth, ΔH_{pp} (in Gauss). The integrated area is obtained by the deconvolution of the spectra using the SimFit software. (c) IR spectra after the adsorption of CO on DND and F-520-DND samples, with an inset showing a magnified view (20×) of the F-520-DND spectrum.

Open Access Article. Published on 24 February 2026. Downloaded on 3/17/2026 1:39:49 PM.
This article is licensed under a Creative Commons Attribution 3.0 Unported Licence.

The FTIR-CO characterizations of these materials (DND and F-520-DND) clearly confirm the complexity of the DND surface and its evolution depending on the treatment applied. Indeed, the presence of carbon in an unsaturated hybridization state is clearly evidenced. To the best of our knowledge, such study is reported here for the first time.

3.2.3 Dramatic modification of the chemical/surface properties of fluorinated DNDs. Anticipating that the significant modification of the functional groups of the DNDs through fluorination, as demonstrated by FTIR spectroscopy, can greatly impact the DND' surface properties, especially their hydrophobicity, raw and fluorinated DNDs (F-520-DND) were studied by both standard N_2 physisorption at −196 °C (77 K) and by water adsorption at 25 °C (Fig. 8). Both samples show a shape typical of N_2 adsorption on DNDs (Fig. 8a).[79] The specific surface areas (SSAs), determined by the BET method (in the P/P_0 range of 0.1–0.3), are 283 ± 7 $m^2\ g^{-1}$ and 249 ± 6 $m^2\ g^{-1}$ for DND and F-520-DND, respectively, in the usually reported range of SSA values (Table 2). The slight decrease in the SSA after fluorination can be explained by a modification of the density of the fluorinated DNDs compared to raw DNDs because carbon atoms are replaced by heavier fluorine atoms in F-520-DND. In the low P/P_0 range (see the inset in the log scale), the shift to higher relative pressures for the fluorinated DND samples suggests an enlargement of the micropores due to the gasification of sp^2 carbon upon reaction with F_2 or the elimination of water molecules blocking the N_2 diffusion at the entrance of the pore mouths.[79] In the high-pressure domain (P/P_0 > 0.9), the higher N_2 uptake of F-520-DND suggests a broader mesopore (and macropore) size distribution, originating from the larger interparticular DND porosity after F_2 treatment. It leads to a higher pore volume as measured at P/P_0 = 0.95, with values of 0.82 ± 0.02 and 0.93 ± 0.02 $cm^3\ g^{-1}$ for DNDs and F-520-DND, respectively (Table 2).

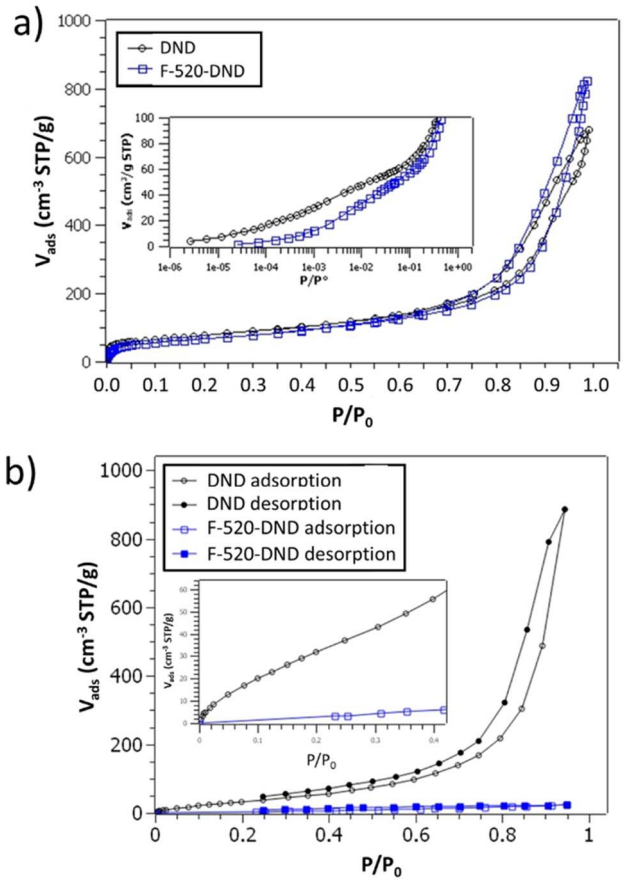

Fig. 8 Gas adsorption on the DND before and after fluorination at 520 °C (F-520-DND): (a) N_2 adsorption/desorption isotherms (−196 °C). (inset) Magnification of the low relative pressure region. (b) Water adsorption/desorption isotherms (25 °C). (inset) Magnification of the low relative pressure region.

The DND and F-520-DND show very different behaviors under H_2O adsorption (Fig. 8b). As expected, the raw DNDs show a specific hydrophilic character, with strongly adsorbed water molecules coexisting with hydrophobic carbon porous features.[80,81] This coexistence gives rise to the large water adsorption/desorption hysteresis observed in a relatively low relative pressure domain (P/P_0 < 0.4). The measured pore volume of raw DNDs (0.71 ± 0.02 $cm^3\ g^{-1}$, determined at P/P_0 = 0.95 and with an adsorbed water density of 1.00 g cm^{-3}) is lower than that measured for N_2 adsorption (0.82 ± 0.02 $cm^3\ g^{-1}$) (Table 2). Similar to what is observed for metal–organic frameworks bearing polar sites (metal–oxygen clusters) and large, very non-polar regions (organic linkers),[82] here, water molecules may preferentially adsorb onto the localized hydrophilic centers such as oxygen-containing functional groups. The latter serve as nucleation sites for the growth and coalescence of water clusters by avoiding adsorption in the pores around the sp^2-carbon hydrophobic domains localized on the DND surface. Hence, the resulting pore volume probed by H_2O adsorption is smaller than that probed by N_2 adsorption. After fluorination, the pore volume of F-520-DND is dramatically reduce to 0.02 ± 0.01 $cm^3\ g^{-1}$ due to the hydrophobic character of the numerous C–F type functions grafted on the DND surface.

To summarize the above results regarding the reactivity of DNDs with F_2, the combination of complementary techniques, among which some were applied to DNDs for the first time, *e.g.,* CO adsorption studied by FTIR, demonstrates the efficiency of the gas/solid fluorination at relatively high temperatures (520 °C) for the elimination of a variety of species from DNDs. The *ex situ* and *in situ* investigations performed during the fluorination of DNDs demonstrate the highly selective reactivity of elemental F_2 towards different kinds of DND impurity including hydrogen-/oxygen-containing functional groups, sp^2 carbon shells and silica even at RT. Clearly, the DND surface is cleaned

Table 2 SSAs and pore volumes from N_2 adsorption isotherms and pore volumes from H_2O adsorption isotherms for raw DNDs (DND) and fluorinated DNDs at 520 °C (F-520-DND).

	N_2 adsorption (−196 °C)		H_2O adsorption (25 °C)
Sample	SSA ($m^2\ g^{-1}$)	Pore volume ($cm^3\ g^{-1}$)	Pore volume ($cm^3\ g^{-1}$)
DND	283 ± 7	0.82 ± 0.02	0.71 ± 0.02
F-520-DND	249 ± 6	0.93 ± 0.02	0.02 ± 0.01

Open Access Article. Published on 24 February 2026. Downloaded on 3/17/2026 1:39:49 PM.
This article is licensed under a Creative Commons Attribution 3.0 Unported Licence.

of hydrogen- and oxygen-containing groups, sp^2 carbon shells, SiO_2 and PC_s at the vicinity of the DND surface while preserving the diamond core of DNDs.

As fluorination is the final step of the purification, it is of importance to investigate the stability of the C–F bonds. Samples which are freshly fluorinated and after 8 years are compared in SI, Fig. S7–S9, evidencing the retention of C–F bonds after such a long period.

3.3 Combination of fluorine and chlorine for highly efficient and complete purification of DNDs

3.3.1 Behavior of metal impurities in DNDs treated under fluorine alone. Iron is one of the main inorganic impurities in DND powders; hence, Mössbauer spectroscopy, although usually not used to study DNDs, is a very relevant technique because it is able to finely probe the chemical environment of iron and helps to determine the iron-based species. It should be pointed out that the low amount of iron present in DNDs forbids its investigation by X-ray photoelectron spectroscopy (XPS). The Mössbauer spectrum of the raw DNDs (Fig. 9a) required a quite long exposure time, *e.g.,* 2 months. It is well fitted with three doublets, indicating the presence of three different oxidation states of Fe in DNDs (Table 3). The observed isomeric shifts correspond to Fe(+III) with two different environments, δ observed at 0.21 and 0.50 mm s^{-1}, in agreement with the reported range of Fe(+III) ions between +0.1 and +0.6 mm s^{-1}, and one environment of Fe(+II) with a δ of +1.15 mm s^{-1}, which is usually reported between +0.7 and +1.5 mm s^{-1}.[83] The Fe(+III) and Fe(+II) of the iron oxides present in DNDs contribute 87% and 13% of the signal, respectively. After fluorination, the Mössbauer features of fluorinated DNDs, F-520-DND (Fig. 9b), are strongly altered. Only one singlet with a chemical shift of +0.39 mm s^{-1} is observed for F-520-DND. It corresponds to superparamagnetic FeF_3.[84–86] HAADF/STEM coupled with EDX spectroscopy elemental mappings was used to detect, localize and locally identify the iron-based impurities present in F-520-DND (SI, Fig. S10). Iron and fluorine, in agreement with the FeF_3 form, have been observed in the same zone, outside the DND agglomerates. Iron accessibility by F_2 is probably favored, leading to their facile fluorination.

The above findings from Mössbauer analysis are of utmost importance to maximize the efficiency of the developed unprecedented purification method. It is indeed obvious that if the F_2 treatment is applied first to raw DNDs, then iron-based impurities cannot be eliminated because they are stabilized in the form of FeF_3 with a high thermal stability. This finding is also evidenced by FTIR analysis of the ashes remaining after the selective combustion[13] of both F-520-DND, referred to as O–F-520-DND, and Cl–F-DND, referred to as O-Cl-F-DND (SI, Fig. S11). The FTIR spectra of O–F-520-DND and O-Cl-F-DND show vibrations of fluorinated metallic compounds, especially Fe–F bonds at around 600 cm^{-1}, in agreement with the presence of FeF_2 and/or FeF_3 compounds.[87,88] The absence of Si–O vibrations is also noticed in the FTIR spectra of O-F-520-DND and O-Cl-F-DND, in agreement with the results of the *in situ* FTIR study during fluorination (SI, Fig. S5). By contrast, the FTIR spectrum of O-Cl-650-DND, resulting from the selective combustion of Cl-650-DND, evidences the elimination of iron- and chromium-type impurities while silica is still present.

3.3.2 Combination of chlorine and fluorine sequential treatment applied to DNDs for their complete purification. Based on the above results, the sequential halogenation treatment applied to DND consisted of chlorination, followed by fluorination. DNDs were then treated under the conditions optimized for both of the halogen-based treatments: *i.e.,* 1 h under Cl_2 at 650 °C with a Cl_2 flow rate of 20 mL min^{-1} (see Section 3.1) and then under F_2 for 12 h at 520 °C (see Section 3.2). The resulting sample, F-Cl-DND (Cl-650-DND fluorinated), was investigated by several complementary techniques and compared to previous samples (DND, Cl-650-DND and F-520-DND) to assess both surface cleaning and inorganic impurity elimination.

First, solid-state MAS-NMR spectroscopy of ^1H, ^{13}C and ^{19}F nuclei was performed on the four samples, DND, Cl-650-DND,

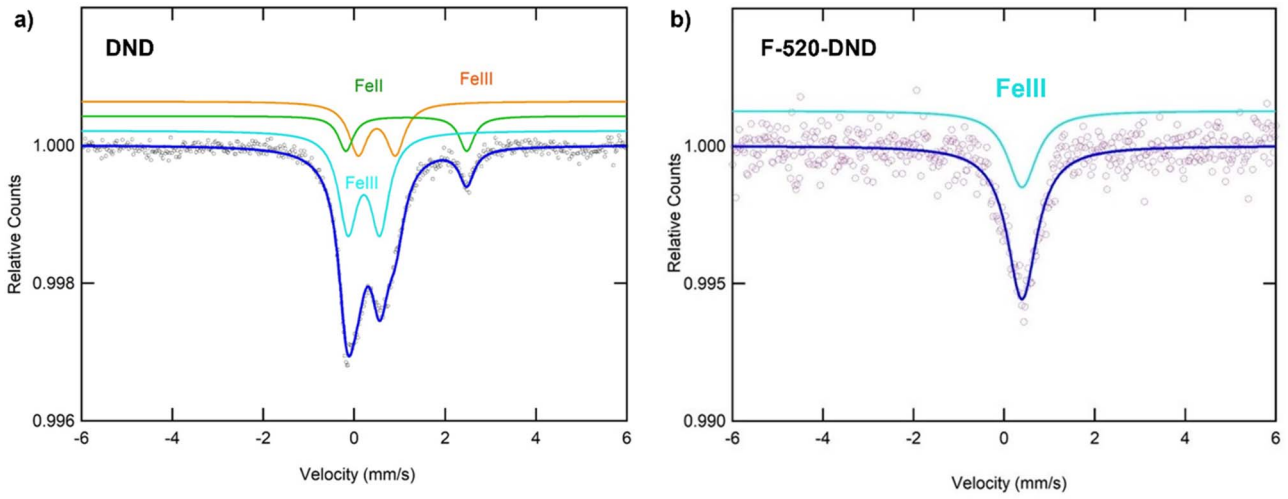

Fig. 9 Mössbauer spectra of (a) raw DNDs (DND) and (b) DNDs fluorinated for 12 h at 520 °C (F-520-DND).

Open Access Article. Published on 24 February 2026. Downloaded on 3/17/2026 1:39:49 PM.
This article is licensed under a Creative Commons Attribution 3.0 Unported Licence.

Table 3 Hyperfine interactions (isomer shift (δ), quadripolar splitting (E_Q) and full width at half-maximum (Δ)) from the Mössbauer spectra of raw DNDs and F-520-DND (DNDs fluorinated for 12 h at 520 °C) samples, with indication of the Fe oxidation state (O.S.)[a]

DND		δ (mm s^{-1})	E_Q (mm s^{-1})	Δ (mm s^{-1})	%	O.S.
Site 1	Doublet	0.21	0.70	0.50	57	Fe (+III)
Site 2	Doublet	0.50	0.82	0.50	30	Fe (+III)
Site 3	Doublet	1.15	2.66	0.40	13	Fe (+II)
F-520-DND	Singlet	0.39	—	0.70	100	Fe (+III)

[a] δ = isomeric shift; E_Q = quadripolar splitting; Δ = FWHM.

F-520-DND and F-Cl-DND (Fig. 10). For a better understanding of the spectra, ^{1}H–^{13}C and ^{13}C–^{19}F cross-polarization MAS-NMR spectra were acquired as well (Fig. 10c). In ^{1}H MAS-NMR spectra (Fig. 10a), the signals of F-Cl-DND and Cl-650-DND (closer to the spectrum of the empty rotor) have a very weak intensity compared with that of DND.

The ^{13}C spectrum of DND consists mainly of the C diamond band (the chemical shift at 35 ppm) with a shoulder at around 75 ppm relating to C–OH bonds[11,89,90] (Fig. 10b). The presence of the C–H bond at 50 ppm is expected because a signal is detected during ^{1}H MAS-NMR. After chlorination is applied to DNDs, the corresponding ^{13}C NMR spectrum is slightly modified with a shoulder in addition to the C–H feature noticeable in the range of 40–60 ppm. The band at 140 ppm can be assigned to sp^2-hybridized C bonded to another sp^2 C.[89–91] When DNDs undergo a fluorination treatment, a shoulder at around 42 ppm, relating to C–C–F bonds, and the C–F band at around 88 ppm are observed, as expected.[11,30] The spectrum of F-Cl-DND consists mainly of the C diamond band (35 ppm) with a C–C–F bond shoulder (42 ppm) and the C–F bond (88 ppm). C–C–F means that the first C with sp^3 hybridization is near a C–F bond. The C–F signal exhibits a greater intensity in F-Cl-DND than in F-520-DND, implying that the chlorination of DND creates additional grafting sites for fluorine than in DNDs in the raw state. It should also be noted that the fluorination of Cl-650-DND completely removes the sp^2 C present on the sample because no signal around 140 ppm is detected for F-Cl-DND.

The ^{1}H–^{13}C CP MAS-NMR spectra of DND, Cl-650-DND and F-Cl-DND are shown in Fig. 10c (no hydrogen detected in F-520-DND). As expected, the ^{1}H–^{13}C CP MAS-NMR spectrum of DND is composed of the C diamond band (35 ppm), C–H bond (42 ppm) and C–OH bond (75 ppm). In the case of Cl-650-ND, the ^{1}H → ^{13}C CP spectrum is much less defined than that of DND; however, the presence of C–H bonds belonging to C–OH bonds is evidenced. This implies that chlorination partially removes hydrogenated groups on the DND surface. The band observed

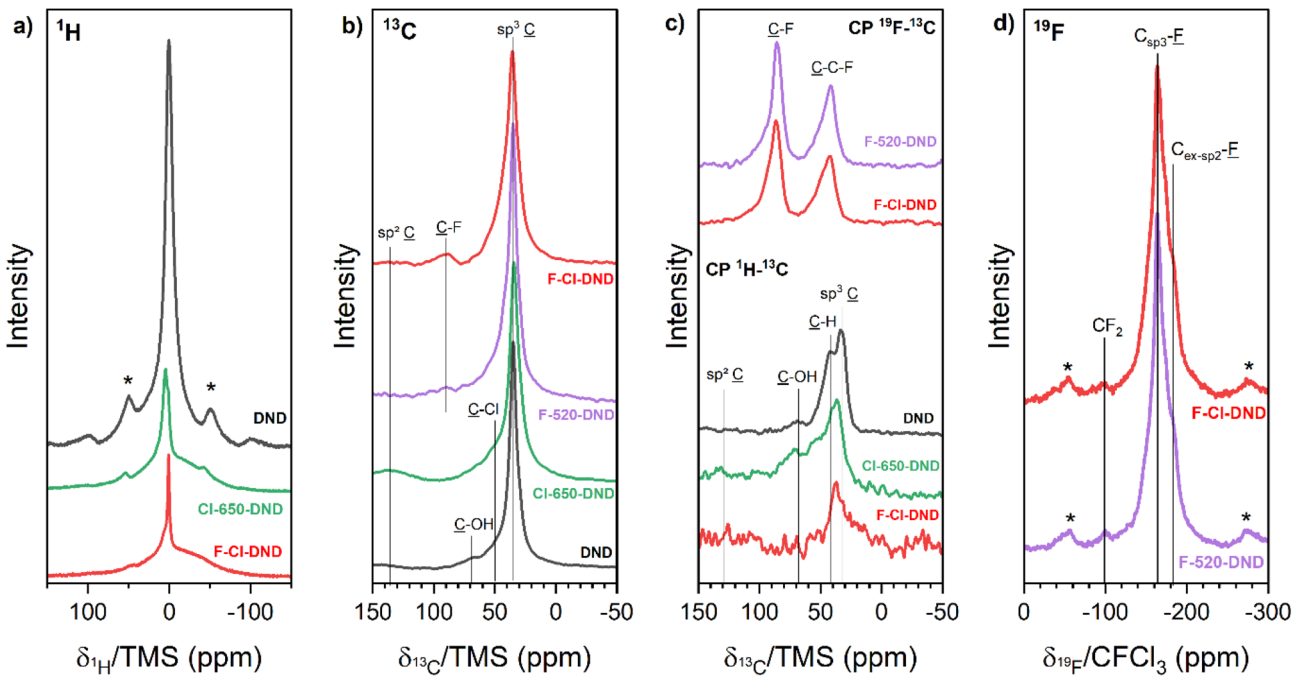

Fig. 10 (a) ^{1}H, (b) ^{13}C, (c) CP ^{19}F → ^{13}C and CP ^{1}H → ^{13}C and (d) ^{19}F MAS-NMR spectra of DND (raw DNDs), Cl-650-DND (DNDs chlorinated at 650 °C for 1 h with a Cl_2 flow rate of 20 mL min^{-1}), F-520-DND (DNDs fluorinated for 12 h at 520 °C), and F-Cl-DND (DNDs chlorinated at 650 °C for 1 h flow rate of 20 mL min^{-1} and fluorinated for 12 h at 520 °C).

Open Access Article. Published on 24 February 2026. Downloaded on 3/17/2026 1:39:49 PM.
This article is licensed under a Creative Commons Attribution 3.0 Unported Licence.

between 50 and 60 ppm can be attributed to the C–Cl bond, according to Panich *et al.*[91] The $^{1}H \rightarrow {}^{13}C$ CP spectrum of F-Cl-DND is noisy despite the long acquisition time used (8 h), revealing the presence of very few hydrogens in the sample, contrary to raw DNDs. The $^{19}F \rightarrow {}^{13}C$ CP-MAS spectrum of F-Cl-DND resembles that of F-520-DND (Fig. 10c), and it shows only the C–C–F and C–F bands at 42 and 86 ppm, respectively, which is in agreement with the above investigations. Finally, the ^{19}F spectrum (Fig. 10d) of the F-Cl-DND is similar to that of F-520-DND, with the presence of C–F (−164 ppm) and C_{ex-sp^2}-F (−182 ppm) bonds originating from the fluorination of C–H/C–OH and sp^2 C, respectively.[11,30] CF_2 groups, in very small quantities, are also evidenced by the band observed at −100 ppm.

In addition to recording the MAS NMR spectra, a careful and rigorous fit of the ^{13}C and ^{19}F spectra (shown in Fig. 10) allowed us to quantify each species/bond from its corresponding contribution to the spectra (Fig. 11).

First, in agreement with the literature,[92,93] the ^{13}C MAS-NMR spectrum of raw DNDs can be well fitted with three contributions of chemical shifts of 35, 50 and 75 ppm, corresponding to sp^3 C bonded to other sp^3 C (diamond core), H atoms in both C–H and CH_3 groups, and C–OH groups, respectively (Fig. 11a). After chlorination only, the ^{13}C MAS-NMR spectrum of Cl-650-ND reveals the presence of the C–Cl band at 50 ppm (at a position close to that of the C–H bond) and confirms the sp^2 C signal at 140 ppm (Fig. 11b).[91,93] The reaction of DNDs with chlorine induces the grafting of Cl atoms on the diamond and the formation of graphitic species. After the fluorination reaction, the ^{13}C MAS-NMR spectrum of F-520-DND (Fig. 11c) shows (i) two bands at 42 and 85 ppm, corresponding to the sp^3 C bonded to C–F (C–C–F) and C–F bonds (C–F), respectively, and (ii) the removal of C–H and C–OH groups. The C–F band is, in fact, a doublet composed of C–F groups grafted onto the diamond bulk (85 ppm) and onto the sp^2 C shell (denoted as C_{ex-sp^2}-F) located at 90 ppm. The latter C–F bond feature is also noticed in the ^{19}F MAS-NMR spectrum (Fig. 11d); the C_{ex-sp^2}-F band appears as a shoulder at −185 ppm, and the C_{sp^3}-F feature is detected at −164 ppm. The CF_2 signal at −140 ppm is not considered for this fit. It is observed that the C_{ex-sp^2}-F signal is less intense than the C_{sp^3}-F signal in both ^{13}C and ^{19}F MAS-NMR spectra. These assignments are in perfect agreement with the ^{13}C MAS-NMR spectrum of F-520-DND and with the literature.[93] From the fit of the ^{13}C spectrum, an F/C ratio of 0.03 is found for F-520-DND, which corresponds to 7.2 wt% of fluorine. Thus, the sp^3 C neighbors of C–F (C–C–F, 4.3 wt%, green) are fewer in F-520-DND than in the diamond (92.8 wt%, blue). The C–F bonds on the diamond surface, which result from both the conversion of C–OH and C–H groups (C–F, at 85 ppm, purple) and from C sp^2 fluorination (C_{ex-sp^2}-F, at 90 ppm, yellow), are present in 2.8 wt% and 0.1 wt%, respectively.

The deconvolution of non-treated and halogenated DNDs allows us to better understand the MAS-NMR spectra of a DND sample submitted to Cl_2 and F_2 treatments. Indeed, according to the fit of the ^{13}C MAS-NMR spectrum of F-Cl-DND (DNDs that were first chlorinated and then fluorinated), the C–Cl bonds coexist with C–F bonds (both fluorine grafted to sp^3 C and C_{ex-sp^2}), as evidenced by the fit (Fig. 11e). These findings are in agreement with the ^{19}F MAS-NMR spectrum of F-520-DND (Fig. 11f). In addition, the signal from C–H is no longer present, in agreement with the very low intensity of the ^{1}H MAS-NMR spectrum of F-Cl-DND (Fig. 10a).

The agglomerated morphology of the DNDs does not seem to pose a significant barrier to the diffusion of halogenated reactants. As expected from our previous work,[94] Cl_2 and F_2 gaseous reactants can permeate the agglomerates and react with species present at the DND surface and at internanodiamond interfaces, while the crystalline diamond core is expected to remain largely unaffected, as evidenced by TEM observations (SI, Fig. S12) and in agreement with the XRD of fluorinated DNDs (SI, Fig. S7). Conversely, the chemistry of the DND surface is shown to be strongly modified after the sequential purification process. Most of the native hydrogen- and oxygen-containing functional groups and the disordered sp^2-C surrounding layer are replaced by fluorine groups, as also evidenced by visual dispersion tests (SI, Fig. S13).

The results of the above NMR study and the complementary characterizations described in this work allow us to propose a comprehensive mechanism leading to purification and halogenation of the DND surface by chlorination, fluorination and the here-developed sequential chlorine-fluorine treatment (Fig. 12).

3.3.3. Influence of the halogen-based treatment on the thermal stability of DNDs. It is well known that surface chemistry and the presence of impurities significantly impact the thermal stability of any material. The efficient removal of both organic and carbon-based impurities is strongly supported by the above results, and additional FTIR investigations of DND, Cl-650-DND, F-520-DND and F-Cl-DND (SI, Fig. S14) show that the applied halogenation treatment induces the grafting of C–F groups on F-Cl-DND, and C–F bonds are well evidenced for F-520-DND. Fig. 13 shows the thermograms under air and the corresponding derivative curves of raw DND, Cl-650-DND, F-520-DND and F-Cl-DND. First, a significant increase in the combustion temperature (T_{comb}) is observed for F-520-DND compared to DND and Cl-650-DND (Fig. 13a). The weight loss in the 550–620 range noticed in the F-520-DND thermogram is certainly due to the release of fluorine *via* a defluorination process. As mentioned before (Section 3.1), the combustion of DNDs can be described by a two-step process, observed as two peaks in the derivative representation (Fig. 13b). Without discussing the detailed shape of the thermogram, raw DNDs burn off at around 500 °C, while chlorination increases the combustion temperature by about 50 °C. The fluorinated DNDs, F-520-DND, are even more stable under air than the chlorinated DNDs, and their thermal stability reaches around 600 °C, at which they start to be gasified after having lost their fluorine-containing groups. The DND treated by our purification/surface cleaning method, F-Cl-DND, shows a substantial improvement in its resistance to oxidation because it can sustain 730 °C under dry air, and the improvement measured here is +225 °C compared to the raw DNDs. Its defluorination, less pronounced than that for F-520-DND, is noticed at around 620 °C. Further, the combustion process occurs in a narrower temperature domain for F-Cl-DND than that observed for the

Open Access Article. Published on 24 February 2026. Downloaded on 3/17/2026 1:39:49 PM.
This article is licensed under a Creative Commons Attribution 3.0 Unported Licence.

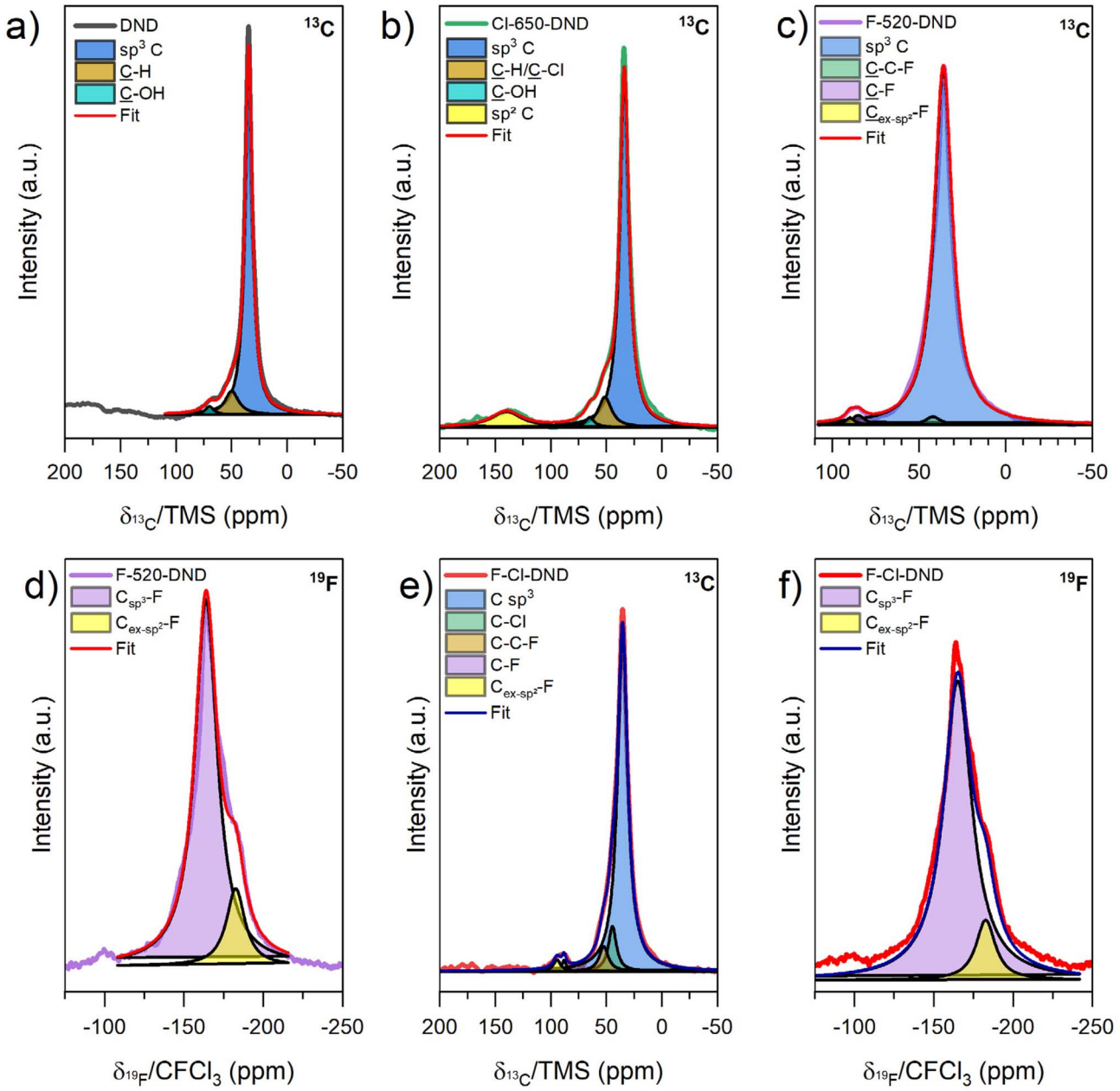

Fig. 11 ^{13}C MAS NMR spectra of (a) DND (raw DNDs), (b) Cl-650-DND (DNDs chlorinated at 650 °C for 1 h with a Cl_2 flow rate of 20 mL min^{-1}), (c) F-520-DND (DNDs fluorinated for 12 h at 520 °C) and (e) F-Cl-DND (DNDs chlorinated at 650 °C for 1 h flow rate of 20 mL min^{-1} and fluorinated for 12 h at 520 °C). ^{19}F MAS-NMR spectra of (d) F-520-DND and (f) F-Cl-DND. The fits were performed with Lorentzian functions. The spinning rates were 10 and 30 kHz for the ^{13}C and ^{19}F NMR, respectively. Spinning sidebands are marked with *.

other studied DNDs. A faster and better-controlled combustion process is probably the signature of better control over the surface properties and fewer different types of functions by efficient surface cleaning after fluorination.

DNDs have been reported as catalysts or catalyst supports in various reactions[95] and are well-suited for harsh condition reactions due to their high core stability. Recent patents further demonstrate their use in HF-based fluorination reactions, highlighting the stability of their specific surface area and the presence of surface vacancies potentially acting as Lewis acid sites involved in Cl/F exchange mechanisms.[96] In this context, the purified and surface-cleaned DNDs investigated in the present study may exhibit distinct catalytic properties owing to their expected stability under HF flow conditions.

4. Discussion

Chlorination first removes metal impurities, while fluorination eliminates the sp^2 carbon shell surrounding the diamond core of DNDs and the hydrogen-/oxygen-containing functional groups (C–H and C–OH), SiO_2 and PCs close to the surface. Because DNDs have a nanometer size, their surface accessible to gas accounts for

Open Access Article. Published on 24 February 2026. Downloaded on 3/17/2026 1:39:49 PM.
This article is licensed under a Creative Commons Attribution 3.0 Unported Licence.

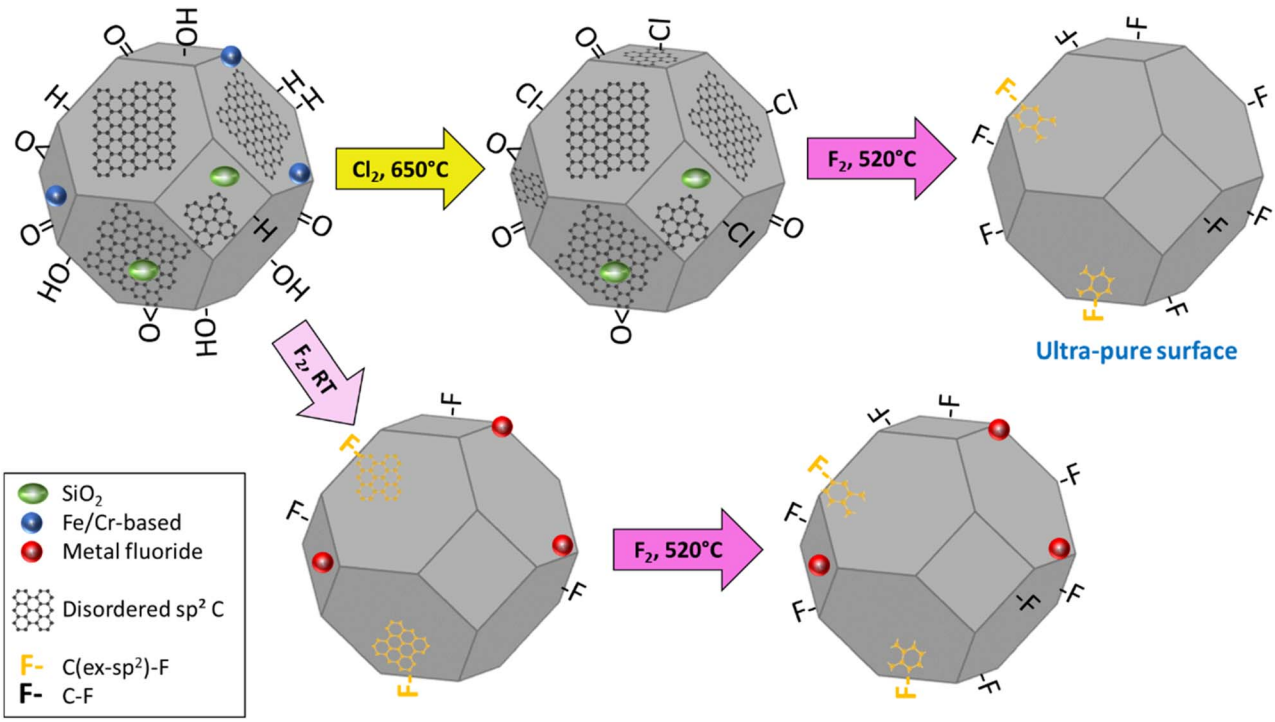

Fig. 12 Complete representation of the purification mechanisms of DND particles by chlorination and fluorination treatments.

a non-negligible part of the sample, which also contributes to their effectiveness. Among all the DND impurities, only nitrogen located within the diamond core of DNDs cannot be reached. The in-depth characterization provided demonstrates the ultrapurity of DNDs after their reaction with chlorine and fluorine. In addition, the purity of the Cl_2–F_2-treated DNDs can be proved by another powerful approach: around 100 mg of the F-Cl-DND powder was burnt off in air according to the selective combustion method described in (ref. 13), and no residue was obtained after combustion, providing crucial evidence of the high efficiency of the developed purification method.

Compared to the initial DND powder, the combustion temperature is upshifted by 225 °C after the developed two-step halogen combined method. Such a difference mainly originates from a modification in the surface chemistry of DNDs. This phenomenon is assumed to be related to the metastability of the diamond phase, which is magnified at the nanometric size. The conversion of diamond into graphite is favored for nanodiamonds in the temperature range used (the presence of sp^2 C at 135 ppm in the ^{13}C NMR spectrum of Cl-650-DND, Fig. 10). When the sp^2 carbons present at the DND surface are burnt off and released as CO and CO_2 gases, the newly exposed diamond

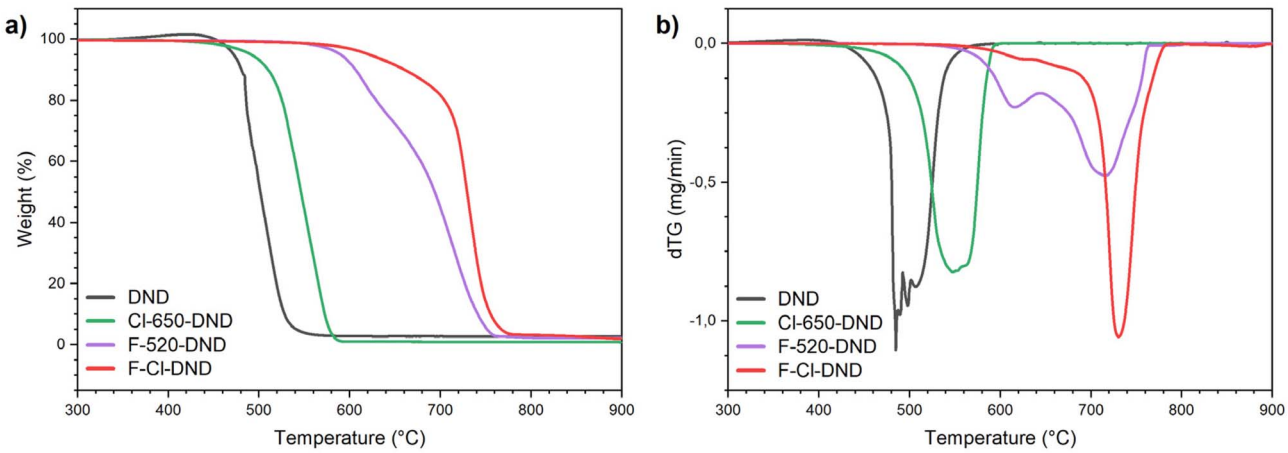

Fig. 13 (a) Thermograms from TGA under a dry air atmosphere for DND (raw DNDs), Cl-650-DND (DNDs chlorinated at 650 °C for 1 h with a Cl_2 flow rate of 20 mL min^{-1}), F-520-DND (DNDs fluorinated for 12 h at 520 °C) and F-Cl-DND (DNDs chlorinated at 650 °C for 1 h flow rate of 20 mL min^{-1} and fluorinated for 12 h at 520 °C) and (b) their corresponding derivative curves.

Open Access Article. Published on 24 February 2026. Downloaded on 3/17/2026 1:39:49 PM.
This article is licensed under a Creative Commons Attribution 3.0 Unported Licence.

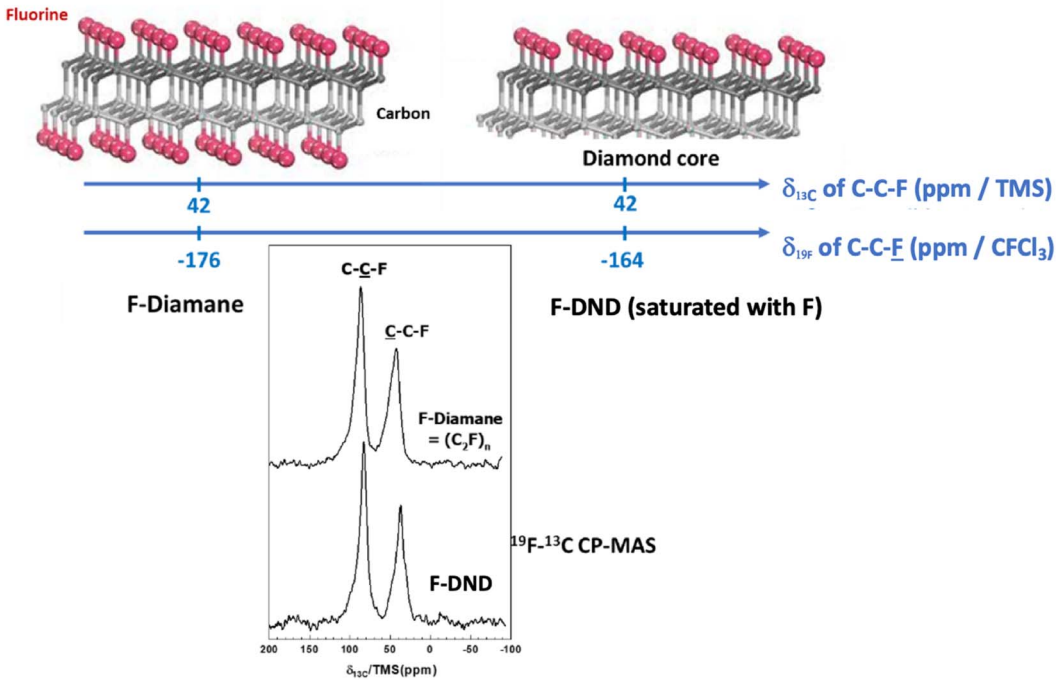

Fig. 14 Chemical shifts of C–C–F and C–C–F groups in the $^{19}F \rightarrow {}^{13}C$ CP-MAS spectrum of fluorinated diamane and F-520-DND. The chemical shifts of these contributions in ^{19}F NMR are also shown.

carbons are converted into sp^2 C instantaneously (the strength of the C–C bond is 347 kJ mol^{-1} instead of 614 kJ mol^{-1} for the C═C bond). Combustion takes place from one step to the next until the completion of the burning process. When fluorine atoms are present on the DND surface, the stability in air is enhanced. To stabilize the diamond phase on the surface and hence maintain the sp^3 structure, the presence of C–F bonds is essential. C–F groups correspond to the fluorine atoms bonded to the diamond and not located in the residual phase C_{ex-sp^2}-F. An analogy with diamane can be made here. Diamane is a 2D structure involving only a bilayer of C with sp^3 hybridization over a large surface area. Preparing low-dimensional diamond-like structures is extremely complex. Unlike graphite, which can be exfoliated into graphene, diamond has a 3D crystal conformation. A high transformation barrier makes diamond metastable and able to exist on geological time scales. However, as the structural dimensions of diamond decrease, surface effects begin to play a major role in a way that cannot be described by the canonical diamond-graphite phase diagram. For diamond structures with dimensions approaching those of the diamond unit cell, the absence of passivating atoms (*e.g.,* fluorine) shifts the phase equilibrium, leading to a significant increase in the graphene–diamond transition pressure and even the disappearance of stability regions for diamonds.[97–99] This is the reason why conventional chemical vapor deposition (CVD) does not allow the synthesis of diamond films of atomic thickness. Since 2009, numerous studies have focused on diamane synthesis, whether by compressing a few graphene layers at high pressure (160–240 GPa),[100–108] using a hot filament process,[109] or by a "chemically induced phase transition" to convert stacked few-layer graphene in an AB mode into stable diamane by sufficient coverage of passivating surface atoms on both free surfaces.[98,108,110–112] Diamane-type materials have been prepared by the fluorination (F-diamane)[105] or hydrogenation[106] of graphene or multilayer graphene films. In the case of fluorinated diamane (F-diamane), fluorine atoms "passivate" the diamane sheets, enabling them to exist at ambient pressure and temperature, thus maintaining the sp^3 hybridization despite the metastable nature of the diamane sheets. The F-diamane structure shown in Fig. 14 can be compared to a layer in the $(C_2F)_n$ phase of fluorinated graphites. The comparison between F-diamane and fluorinated DND is supported by the close chemical shifts in ^{13}C NMR (42 ppm for C–C–F) and ^{19}F NMR (−164 or −176 ppm C–C–F) (Fig. 14). If we liken the nanodiamond surface to a curved diamane layer missing half its fluorine atoms (on the diamond core side), the fluorine atoms "passivate" the diamond surface and fix the sp^3 hybridization of the carbon atoms. The thermal removal of the fluorine atoms induces a phase change from metastable diamond to graphite. It should be noted that diamane passivation can theoretically be achieved by hydroxyl groups and hydrogen. It is therefore not aberrant to observe the graphitization of DND by chlorination in the used temperature range if we consider the eventual ablation of C–OH and C–H.

5. Conclusion

DNDs with an ultrapure surface were prepared by a combination of gas/solid halogenations. We demonstrated that the combined chlorine-fluorine treatment is a powerful purification method for DNDs. First, chlorination with pure Cl_2 gas at 650 °C for 1 h is able to remove metal impurities by forming volatile

Open Access Article. Published on 24 February 2026. Downloaded on 3/17/2026 1:39:49 PM.
This article is licensed under a Creative Commons Attribution 3.0 Unported Licence.

metal chlorides. Then, fluorination with pure F_2 at 520 °C for 12 h is able to remove the remaining SiO_2 impurities, the sp^2 carbon shell, and the hydrogenated and oxygenated groups (C–OH and C–H) through the release of SiF_4, CF_4 (and other gaseous C_xF_y) and HF, respectively, all in gaseous states. Fluorination allows the removal of the paramagnetic centers close to the DND surface. Only nitrogen located within the diamond core cannot be removed by this purification method. Both F_2 and Cl_2 do not react with the diamond core and cannot diffuse deeply in the DND particles, which provides a highly selective purification treatment with highly efficient elimination of nondiamond species. Moreover, the DNDs cleaned of all their external impurities show a high hydrophobic character thanks to the presence of fluorine atoms on their surface. The adsorption of water molecules is hence avoided, leading to very stable DNDs under atmospheric conditions. The fluorine atoms provide another important benefit: the thermal stability in air is drastically enhanced, with a remarkable combustion temperature upshift of 225 °C (compared with the raw DND). By comparison with fluorinated diamane, F atoms passivate the diamond surface and fix the sp^3 hybridization on the surface. The rebuilding of the surface with a conversion of metastable diamonds into graphite-like shells is avoided. The proposed combination of halogenations cleans the DND surface and erases the history of both synthesis and preliminary purification processes. Hence, the problem of homogeneity between batches can be resolved. The DND surface is clean and uniform for applications, such as heterogeneous catalysis, performed under harsh environmental conditions.

Author contributions

K. H.: data curation, formal analysis, investigation, methodology, visualization, writing – original draft, writing – review & editing. M. E., S. D., S. H., J. P. and J.-D. C.: data curation, formal analysis, investigation and writing – original draft. S. B.: validation, visualization, writing – review & editing. M. D. and B. V.: conceptualization, data curation, funding acquisition, methodology, project administration, resources, supervision, validation, visualization, writing – original draft, writing – review & editing.

Conflicts of interest

The authors declare no competing interests.

Data availability

The data supporting this article have been included as part of the supplementary information (SI). Supplementary information: 1. optimization of the chlorine-based treatment including: optimization of the duration of the chlorine-based treatment, optimization of the Cl_2 flowrate and modelization of the DND thermograms and 2. optimization of fluorine purification treatment including: exothermic reaction at ambient temperature, *in situ* gas phase FTIR study, investigation of paramagnetic defects of DNDs by EPR, a literature review, investigation of the long-term stability of fluorinated DND, study of the influence of fluorination on metallic impurities of fluorinated DNDs, nanodiamond core *vs.* nanodiamond surface modification and surface modification of F-Cl-DND. See DOI: https://doi.org/10.1039/d5ta08349d.

Acknowledgements

This research was funded by the ANR-20-CE08-0034 grant (France). We thank Cyril Vaulot and Habiba Nouali for adsorption analyses performed on IS2M Mulhouse technical platforms. The authors would like to thank Lionel Aranda for his help during TGA experiments.

References

1 V. N. Mochalin, O. Shenderova, D. Ho and Y. Gogotsi, *Nat. Nanotechnol.*, 2012, **7**, 11–23.
2 M. Baidakova and A. Vul', *J. Phys. D: Appl. Phys.*, 2007, **40**, 6300–6311.
3 V. Y. Dolmatov, *Russ. Chem. Rev.*, 2001, **70**, 607–626.
4 V. Yu. Dolmatov, A. N. Ozerin, I. I. Kulakova, O. O. Bochechka, N. M. Lapchuk, V. Myllymäki and A. Vehanen, *Russ. Chem. Rev.*, 2020, **89**, 1428–1462.
5 H. Wang and Y. Cui, *Carbon Energy*, 2019, **1**, 13–18.
6 A. M. Schrand, S. A. C. Hens and O. A. Shenderova, *Crit. Rev. Solid State Mater. Sci.*, 2009, **34**, 18–74.
7 K. Turcheniuk and V. N. Mochalin, *Nanotechnology*, 2017, **28**, 252001.
8 K. J. van der Laan, M. Hasani, T. Zheng and R. Schirhagl, *Small*, 2018, **14**, 1703838.
9 A. M. Schrand, H. Huang, C. Carlson, J. J. Schlager, E. Ōsawa, S. M. Hussain and L. Dai, *J. Phys. Chem. B*, 2007, **111**, 2–7.
10 V. V. Nesvizhevsky, E. V. Lychagin, A. Yu. Muzychka, A. V. Strelkov, G. Pignol and K. V. Protasov, *Nucl. Instrum. Methods Phys. Res., Sect. A*, 2008, **595**, 631–636.
11 V. Nesvizhevsky, U. Köster, M. Dubois, N. Batisse, L. Frezet, A. Bosak, L. Gines and O. Williams, *Carbon*, 2018, **130**, 799–805.
12 A. T. Dideikin, in *Detonation Nanodiamonds*, Jenny Stanford Publishing, 2013.
13 K. Henry, M. Emo, S. Diliberto, S. Hupont, J.-C. Arnault, H. Girard, M. Dubois and B. Vigolo, *Diamond Relat. Mater.*, 2023, **140**, 110466.
14 V. Pichot, M. Comet, E. Fousson, C. Baras, A. Senger, F. Le Normand and D. Spitzer, *Diamond Relat. Mater.*, 2008, **17**, 13–22.
15 A. M. Panich, N. A. Sergeev and S. D. Goren, *Solid State Nucl. Magn. Reson.*, 2020, **105**, 101624.
16 *Detonation Nanodiamonds: Science and Applications*, ed. A. Vul' and O. Shenderova, Jenny Stanford Publishing, New York, 2014.
17 R. Yu. Yakovlev, N. N. Dogadkin, I. I. Kulakova, G. V. Lisichkin, N. B. Leonidov and V. P. Kolotov, *Diamond Relat. Mater.*, 2015, **55**, 77–86.

 This journal is © The Royal Society of Chemistry 2026

Open Access Article. Published on 24 February 2026. Downloaded on 3/17/2026 1:39:49 PM.
This article is licensed under a Creative Commons Attribution 3.0 Unported Licence.

18 V. Yu. Dolmatov, A. Vehanen, V. Myllymäki, K. A. Rudometkin, A. N. Panova, K. M. Korolev and T. A. Shpadkovskaya, *J. Superhard Mater.*, 2013, **35**, 408–414.
19 V. Yu. Dolmatov, M. V. Veretennikova, V. A. Marchukov and V. G. Sushchev, *Phys. Solid State*, 2004, **46**, 611–615.
20 V. G. Sushchev, V. Yu. Dolmatov, V. A. Marchukov and M. V. Veretennikova, *J. Superhard Mater.*, 2008, **30**, 297–304.
21 D. P. Mitev, A. T. Townsend, B. Paull and P. N. Nesterenko, *Diamond Relat. Mater.*, 2014, **48**, 37–46.
22 I. Petrov, O. Shenderova, V. Grishko, V. Grichko, T. Tyler, G. Cunningham and G. McGuire, *Diamond Relat. Mater.*, 2007, **16**, 2098–2103.
23 A. V. Tyurnina, I. A. Apolonskaya, I. I. Kulakova, P. G. Kopylov and A. N. Obraztsov, *J. Surg. Invest.*, 2010, **4**, 458–463.
24 N. Berrada, A. Desforges, C. Bellouard, E. Flahaut, J. Gleize, J. Ghanbaja and B. Vigolo, *J. Phys. Chem. C*, 2019, **123**, 14725–14733.
25 A. Desforges, A. V. Bridi, J. Kadok, E. Flahaut, F. Le Normand, J. Gleize, C. Bellouard, J. Ghanbaja and B. Vigolo, *Carbon*, 2016, **110**, 292–303.
26 G. Mercier, C. Hérold, J.-F. Marêché, S. Cahen, J. Gleize, J. Ghanbaja, G. Lamura, C. Bellouard and B. Vigolo, *New J. Chem.*, 2013, **37**, 790–795.
27 E. Remy, S. Cahen, B. Malaman, J. Ghanbaja, C. Bellouard, G. Medjahdi, A. Desforges, S. Fontana, J. Gleize, B. Vigolo and C. Herold, *Carbon*, 2015, **93**, 933–944.
28 E. L. K. Chng, H. L. Poh, Z. Sofer and M. Pumera, *Phys. Chem. Chem. Phys.*, 2013, **15**, 5615–5619.
29 B. V. Spitsyn, J. L. Davidson, M. N. Gradoboev, T. B. Galushko, N. V. Serebryakova, T. A. Karpukhina, I. I. Kulakova and N. N. Melnik, *Diamond Relat. Mater.*, 2006, **15**, 296–299.
30 A. M. Panich, H.-M. Vieth, A. I. Shames, N. Froumin, E. Ôsawa and A. Yao, *J. Phys. Chem. C*, 2010, **114**, 774–782.
31 Y. Liu, Z. Gu, J. L. Margrave and V. N. Khabashesku, *Chem. Mater.*, 2004, **16**, 3924–3930.
32 M. Herraiz, N. Batisse, M. Dubois, V. V. Nesvizhevsky, C. Cavallari, M. Brunelli, V. Pischedda and S. Radescu, *J. Phys. Chem. C*, 2020, **124**, 14229–14236.
33 E. M. Zagrebina, A. V. Generalov, A. Yu. Klyushin, K. A. Simonov, N. A. Vinogradov, M. Dubois, L. Frezet, N. Mårtensson, A. B. Preobrajenski and A. S. Vinogradov, *J. Phys. Chem. C*, 2015, **119**, 835–844.
34 V. Yu. Osipov, N. M. Romanov, K. Kogane, H. Touhara, Y. Hattori and K. Takai, *Mendeleev Commun.*, 2020, **30**, 84–87.
35 J. Havlik, H. Raabova, M. Gulka, V. Petrakova, M. Krecmarova, V. Masek, P. Lousa, J. Stursa, H.-G. Boyen, M. Nesladek and P. Cigler, *Adv. Funct. Mater.*, 2016, **26**, 4134–4142.
36 V. N. Khabashesku, W. E. Billups and J. L. Margrave, *Acc. Chem. Res.*, 2002, **35**, 1087–1095.
37 Y. Wang, H. Huang, J. Zang, F. Meng, L. Dong and J. Su, *Int. J. Electrochem. Sci.*, 2012, **7**, 6807–6815.
38 A. Krueger, in *Nanodiamonds*, ed. J.-C. Arnault, Elsevier, 2017, pp. 183–242.
39 M. Herraiz, N. Batisse, M. Dubois, V. V. Nesvizhevsky, C. Cavallari, M. Brunelli, V. Pischedda and S. Radescu, *J. Phys. Chem. C*, 2020, **124**, 14229–14236.
40 A. Aleksenskii, M. Bleuel, A. Bosak, A. Chumakova, A. Dideikin, M. Dubois, E. Korobkina, E. Lychagin, A. Muzychka, G. Nekhaev, V. Nesvizhevsky, A. Nezvanov, R. Schweins, A. Shvidchenko, A. Strelkov, K. Turlybekuly, A. Vul' and K. Zhernenkov, *Nanomaterials*, 2021, **11**, 1945.
41 A. Bosak, A. Dideikin, M. Dubois, O. Ivankov, E. Lychagin, A. Muzychka, G. Nekhaev, V. Nesvizhevsky, A. Nezvanov, R. Schweins, A. Strelkov, A. Vul' and K. Zhernenkov, *Materials*, 2020, **13**, 3337.
42 V. V. Nesvizhevsky, M. Dubois, Ph. Gutfreund, E. V. Lychagin, A. Yu. Nezvanov and K. N. Zhernenkov, *Phys. Rev. A*, 2018, **97**, 023629.
43 C. Bellouard, G. Mercier, S. Cahen, J. Ghanbaja, G. Medjahdi, J. Gleize, G. Lamura, C. Hérold and B. Vigolo, *J. Magn. Magn. Mater.*, 2016, **411**, 39–48.
44 B. V. Spitsyn, S. A. Denisov, N. A. Skorik, A. G. Chopurova, S. A. Parkaeva, L. D. Belyakova and O. G. Larionov, *Diamond Relat. Mater.*, 2010, **19**, 123–127.
45 L. Stobinski, B. Lesiak, L. Kövér, J. Tóth, S. Biniak, G. Trykowski and J. Judek, *J. Alloys Compd.*, 2010, **501**, 77–84.
46 Y. A. Abdu, F. C. Hawthorne and M. E. Varela, *Astrophys. J. Lett.*, 2018, **856**, L9.
47 M. Chatenet, S. Berthon-Fabry, Y. Ahmad, K. Guérin, M. Colin, H. Farhat, L. Frezet, G. Zhang and M. Dubois, *Adv. Energy Mater.*, 2023, **13**, 2204304.
48 C. M. Roehl, D. Boglu, C. Brühl and G. K. Moortgat, *Geophys. Res. Lett.*, 1995, **22**, 815–818.
49 D. E. Milligan and M. E. Jacox, *J. Chem. Phys.*, 1968, **48**, 2265–2271.
50 J. H. Newton and W. B. Person, *J. Chem. Phys.*, 1978, **68**, 2799–2805.
51 D. E. Milligan, D. E. Mann, M. E. Jacox and R. A. Mitsch, *J. Chem. Phys.*, 1964, **41**, 1199–1203.
52 A. S. Lefohn and G. C. Pimentel, *J. Chem. Phys.*, 1971, **55**, 1213–1217.
53 T. J. Baker, R. G. Tonkyn, C. J. Thompson, M. K. Dunlap, P. G. Koster van Groos, N. A. Thakur, M. J. Wilhelm, T. L. Myers and T. J. Johnson, *J. Quant. Spectrosc. Radiat. Transf.*, 2023, **295**, 108420.
54 J. Ballard, R. J. Knight and D. A. Newnham, *J. Quant. Spectrosc. Radiat. Transf.*, 2000, **66**, 199–212.
55 G. A. Kuipers, D. F. Smith and A. H. Nielsen, *J. Chem. Phys.*, 1956, **25**, 275–279.
56 W. F. Herget, W. E. Deeds, N. M. Gailar, R. J. Lovell and A. H. Nielsen, *J. Opt. Soc. Am.*, 1962, **52**, 1113–1119.
57 S. A. Sandford and L. J. Allamandola, *Astrophys. J.*, 1990, **355**, 357.
58 K. Coenen, F. Gallucci, B. Mezari, E. Hensen and M. van Sint Annaland, *J. CO2 Util.*, 2018, **24**, 228–239.
59 F. Azzolina-Jury and F. Thibault-Starzyk, *Top. Catal.*, 2017, **60**, 1709–1721.
60 R. J. Waltman, *J. Fluorine Chem.*, 2013, **156**, 378–381.

Open Access Article. Published on 24 February 2026. Downloaded on 3/17/2026 1:39:49 PM.
This article is licensed under a Creative Commons Attribution 3.0 Unported Licence.

61 V. C. Papadimitriou and J. B. Burkholder, *J. Phys. Chem. A*, 2016, **120**, 6618–6628.
62 M. J. Hopper, J. W. Russell and J. Overend, *J. Chem. Phys.*, 1968, **48**, 3765–3772.
63 P. J. H. Woltz and A. H. Nielsen, *J. Chem. Phys.*, 1952, **20**, 307–312.
64 M. O. Ishtiak, O. Colebatch, K. Le Bris, P. J. Godin and K. Strong, *J. Mol. Spectrosc.*, 2024, **401**, 111900.
65 A. N. Alcaraz, J. Codnia and M. L. Azcárate, *J. Photochem. Photobiol., A*, 2009, **205**, 79–83.
66 P. Francis, C. Chaffin, A. Maciejewski and C. Oppenheimer, *Geophys. Res. Lett.*, 1996, **23**, 249–252.
67 A. E. Guber and U. Köhler, *J. Mol. Struct.*, 1995, **348**, 209–212.
68 A. I. Shames and A. M. Panich, in *Nanodiamonds*, ed. J.-C. Arnault, Elsevier, 2017, pp. 131–154.
69 A. I. Shames, A. M. Panich, W. Kempiíski, M. V. Baidakova, V. Yu. Osipov, T. Enoki and A. Ya. Vul', in *Synthesis, Properties and Applications of Ultrananocrystalline Diamond*, ed. D. M. Gruen, O. A. Shenderova and A. Ya. Vul, Springer Netherlands, Dordrecht, 2005, pp. 271–282.
70 E. V. Stepanov, S. N. Kotelnikov, A. Y. Stavtsev and S. G. Kasoev, *J. Phys.: Conf. Ser.*, 2020, **1560**, 012053.
71 K. I. Hadjiivanov and G. N. Vayssilov, in *Advances in Catalysis*, Academic Press, 2002, vol. 47, pp. 307–511.
72 M. I. Zaki and H. Knözinger, *Mater. Chem. Phys.*, 1987, **17**, 201–215.
73 T. H. Ballinger and J. T. Jr. Yates, *Langmuir*, 1991, **7**, 3041–3045.
74 E. Kemnitz, *Catal. Sci. Technol.*, 2015, **5**, 786–806.
75 K. Hadjiivanov, O. Saur, J. Lamotte and J.-C. Lavalley, *Z. Phys. Chem.*, 1994, **187**, 281–300.
76 A. Impellizzeri, J. Dieu, J. Rousseau, S. Brunet and C. P. Ewels, *Catal. Sci. Technol.*, 2024, **14**, 3021–3028.
77 S. Wuttke, A. Vimont, J.-C. Lavalley, M. Daturi and E. Kemnitz, *J. Phys. Chem. C*, 2010, **114**, 5113–5120.
78 C. Morterra, G. Cerrato, P. Cuzzato, A. Masiero and M. Padovan, *J. Chem. Soc., Faraday Trans.*, 1992, **88**, 2239–2250.
79 E. Z. Piña-Salazar, K. Sagisaka, T. Hayashi, Y. Hattori, T. Sakai, E. Ōsawa and K. Kaneko, *Nanomaterials*, 2021, **11**, 2772.
80 E.-Z. Piña-Salazar, R. Kukobat, R. Futamura, T. Hayashi, S. Toshio, E. Ōsawa and K. Kaneko, *Carbon*, 2018, **139**, 853–860.
81 M. V. Korobov, N. V. Avramenko, A. G. Bogachev, N. N. Rozhkova and E. Ōsawa, *J. Phys. Chem. C*, 2007, **111**, 7330–7334.
82 P. Küsgens, M. Rose, I. Senkovska, H. Fröde, A. Henschel, S. Siegle and S. Kaskel, *Microporous Mesoporous Mater.*, 2009, **120**, 325–330.
83 J.-P. EYMERY and J. TEILLET, *Techniques de l'Ingénieur*, 1994, p2600.
84 H. Guérault, M. Tamine and J. M. Grenèche, *J. Phys.: Condens. Matter*, 2000, **12**, 9497.
85 D. W. Collins, J. T. Dehn and L. N. Mulay, in *Mössbauer Effect Methodology*, ed. I. J. Gruverman, Springer US, Boston, MA, 1967, pp. 103–122.
86 S. Mørup, H. Topsøe and J. Lipka, *J. Phys., Colloq.c*, 1976, **37**, C6–C290.
87 J. Giordano, E. Alaoui-Bichri, C. Benoit, R. Almairac and A. M. Bon, *J. Phys., Lett.*, 1979, **40**, 153–156.
88 S. Bouketaya, M. Smida, M. S. M. Abdelbaky, M. Dammak and S. García-Granda, *J. Solid State Chem.*, 2018, **262**, 343–350.
89 M. Dubois, K. Guérin, N. Batisse, E. Petit, A. Hamwi, N. Komatsu, H. Kharbache, P. Pirotte and F. Masin, *Solid State Nucl. Magn. Reson.*, 2011, **40**, 144–154.
90 M. Dubois, K. Guérin, E. Petit, N. Batisse, A. Hamwi, N. Komatsu, J. Giraudet, P. Pirotte and F. Masin, *J. Phys. Chem. C*, 2009, **113**, 10371–10378.
91 A. M. Panich, N. A. Sergeev, M. Olszewski, N. Froumin, A. T. Dideykin, V. V. Sokolov and A. Ya. Vul, *J. Nanosci. Nanotechnol.*, 2015, **15**, 1030–1036.
92 A. I. Shames, A. M. Panich, L. Friedlander and V. Yu. Dolmatov, *Diamond Relat. Mater.*, 2023, **136**, 110059.
93 A. M. Panich, *Diamond Relat. Mater.*, 2017, **79**, 21–31.
94 A. Aleksenskii, M. Bleuel, A. Bosak, A. Chumakova, A. Dideikin, M. Dubois, E. Korobkina, E. Lychagin, A. Muzychka, G. Nekhaev, V. Nesvizhevsky, A. Nezvanov, R. Schweins, A. Shvidchenko, A. Strelkov, K. Turlybekuly, A. Vul', K. Zhernenkov, A. Aleksenskii, M. Bleuel, A. Bosak, A. Chumakova, A. Dideikin, M. Dubois, E. Korobkina, E. Lychagin, A. Muzychka, G. Nekhaev, V. Nesvizhevsky, A. Nezvanov, R. Schweins, A. Shvidchenko, A. Strelkov, K. Turlybekuly, A. Vul' and K. Zhernenkov, *Nanomaterials*, 2021, **11**(8), 1945.
95 N. Gupta, Q. Wang, G. Wen and D. S. Su, Nanodiamonds for catalytic reactions, in *Nanodiamonds: Advanced Material Analysis, Properties and Applications*, ed. J. C. Arnault, Elsevier, Amsterdam, 2017, ch. 18, pp. 439–463.
96 E. Perrin, S. Brunet and J. Dieu, Method for fluorinating hydrogen bis(chlorosulfonyl)imide in gas phase, *US Pat.*, 20260001761, 2026.
97 L. Li and X. Zhao, *J. Phys. Chem. C*, 2011, **115**, 22168–22179.
98 A. G. Kvashnin, L. A. Chernozatonskii, B. I. Yakobson and P. B. Sorokin, *Nano Lett.*, 2014, **14**, 676–681.
99 D. Qiu, Z. Zhang, J. Li, S. Cheng and H. Li, *Diamond Relat. Mater.*, 2018, **84**, 55–61.
100 S. M. Clark, K.-J. Jeon, J.-Y. Chen and C.-S. Yoo, *Solid State Commun.*, 2013, **154**, 15–18.
101 F. Ke, L. Zhang, Y. Chen, K. Yin, C. Wang, Y.-K. Tzeng, Y. Lin, H. Dong, Z. Liu, J. S. Tse, W. L. Mao, J. Wu and B. Chen, *Nano Lett.*, 2020, **20**, 5916–5921.
102 F. Ke, Y. Chen, K. Yin, J. Yan, H. Zhang, Z. Liu, J. S. Tse, J. Wu, H. Mao and B. Chen, *Proc. Natl. Acad. Sci. U. S. A.*, 2019, **116**, 9186–9190.
103 Z. Tao, J. Du, Z. Qi, K. Ni, S. Jiang and Y. Zhu, *Appl. Phys. Lett.*, 2020, **116**, 133101.
104 Y. Horbatenko, M. Yousaf, J. Lee, T. H. Choi, R. S. Ruoff and N. Park, *Carbon*, 2016, **106**, 158–163.

 This journal is © The Royal Society of Chemistry 2026

Open Access Article. Published on 24 February 2026. Downloaded on 3/17/2026 1:39:49 PM.
This article is licensed under a Creative Commons Attribution 3.0 Unported Licence.

105 P. V. Bakharev, M. Huang, M. Saxena, S. W. Lee, S. H. Joo, S. O. Park, J. Dong, D. C. Camacho-Mojica, S. Jin, Y. Kwon, M. Biswal, F. Ding, S. K. Kwak, Z. Lee and R. S. Ruoff, *Nat. Nanotechnol.*, 2020, **15**, 59–66.
106 S. Rajasekaran, F. Abild-Pedersen, H. Ogasawara, A. Nilsson and S. Kaya, *Phys. Rev. Lett.*, 2013, **111**, 085503.
107 P. B. Sorokin and B. I. Yakobson, *Nano Lett.*, 2021, **21**, 5475–5484.
108 L. A. Chernozatonskii, P. B. Sorokin, A. G. Kvashnin and D. G. Kvashnin, *JETP Lett.*, 2009, **90**, 134–138.
109 F. Piazza, K. Cruz, M. Monthioux, P. Puech and I. Gerber, *Carbon*, 2020, **169**, 129–133.
110 M. A. Ribas, A. K. Singh, P. B. Sorokin and B. I. Yakobson, *Nano Res.*, 2011, **4**, 143–152.
111 L. Yu. Antipina and P. B. Sorokin, *J. Phys. Chem. C*, 2015, **119**, 2828–2836.
112 D. Odkhuu, D. Shin, R. S. Ruoff and N. Park, *Sci. Rep.*, 2013, **3**, 3276.